Geophysical Journal International

Geophys. J. Int. (2025) **244,** 1–21
Advance Access publication 2025 November 06
Research Paper

https://doi.org/10.1093/gji/ggaf464

Induced polarization as a tool to characterize permafrost. 2. Applications to low and high-porosity environments

A. Revil,[1] P.-A. Duvillard,[2] M. Marcer,[3,4] J. Richard,[1,2] T. Ingeman-Nielsen,[2] F. Abdulsamad,[2] F. Magnin,[1] B. Charonnat,[5] H. Cai,[6,7] X. Hu,[6,7] L. Ravanel[1] and P. Schoeneich[8]

[1] *Université Savoie Mont-Blanc, CNRS, UMR CNRS* 5204*, EDYTEM, 73370 Le Bourget du Lac, France E-mail: andre.revil@univ-smb.fr*
[2] *Naga Geophysics, Technolac, 229 Rue Joseph Fontanet, 73000 Chambéry, France*
[3] *DTU Sustain, Bygning* 119*,* DK-2800 *Kgs. Lyngby, Denmark*
[4] *Arctic DTU, Siimuup Aqqutaa* 32*, B-*1280*,* 3911 *Sisimiut, Greenland*
[5] *École de Technologie Supérieure, 1100, rue Notre-Dame Ouest, Montréal H3C 1K3, Canada*
[6] *School of Geophysics and Geomatics, China University of Geosciences and Hubei Subsurface Multi-scale Imaging Key Laboratory, Wuhan* 430074*, China*
[7] *State Key Laboratory of Geological Processes and Mineral Resources, China University of Geosciences, Wuhan* 430074*, China*
[8] *Université Grenoble Alpes, IUGA, PACTE,* F-38000 *Grenoble, France*

Accepted 2025 November 12. Received 2025 September 9; in original form 2025 June 23

SUMMARY

In the previous paper of this series, a petrophysical model named the Dynamic Stern Layer (DSL) model was extended to describe induced polarization phenomena associated with permafrost by capturing direct and indirect effects associated with the presence of ice in porous media. In this paper, time-domain induced polarization data obtained in field conditions are interpreted thanks to this updated DSL model. We selected three different test sites in order to apply the DSL model to very different conditions of low and high ice contents to see how ice content directly and indirectly affects geoelectrical measurements. A first survey is performed along a cross-section of a ridge in the Kangerlussuaq mountains of Greenland (Site I). In this area, the rock corresponds to a Precambrian granite characterized by a rather low (<5 per cent) porosity and therefore a low ice volumetric content on the North face of the ridge. We do not see any direct ice polarization contribution in the data obtained with a current injection period of 1 s. We also performed a field survey close to Col des Vés (2846 m a.s.l., Tignes, French Alps, Site II). This site corresponds to a complex ground ice body overlying a substratum made of a low-porosity marble, both having high resistivity values. The front of this body is characterized by a small amount of residual ice while the roots are ice-rich. Therefore the porosity at this site is high and the ice content highly variable. This case study showcases the role of ice in the induced polarization data in terms of high chargeability values (close to 1 as predicted by the theory in which ice behaves as a surfacic protonic semiconductor) at the roots of the complex ground ice body. A third site (Site III) corresponds to a profile crossing the Aiguille du Midi (3842 m a.s.l., Chamonix), also in the French Alps in a low porosity granitic environment. Laboratory experiments are used to interpret the tomograms of the electrical conductivity and normalized chargeability using the DSL model and water content and cation exchange capacity tomograms are reconstructed at these sites. This study demonstrates the ability of induced polarization to be an efficient tool to characterize permafrost in very different field conditions.

Key words: Electrical properties; Electrical resistivity tomography (ERT); Induced polarization.

1 INTRODUCTION

In the current context of climate change, hydrogeological and geophysical methods offer valuable techniques to image, characterize and monitor the presence of permafrost at various scales, different temperatures and in situations characterized by different ice contents (e.g. Moore *et al.* 1994; Hauck *et al.* 2003; Kulessa *et al.* 2003, 2005, 2006; Dafflon *et al.* 2016; Abdulsamad *et al.* 2019,

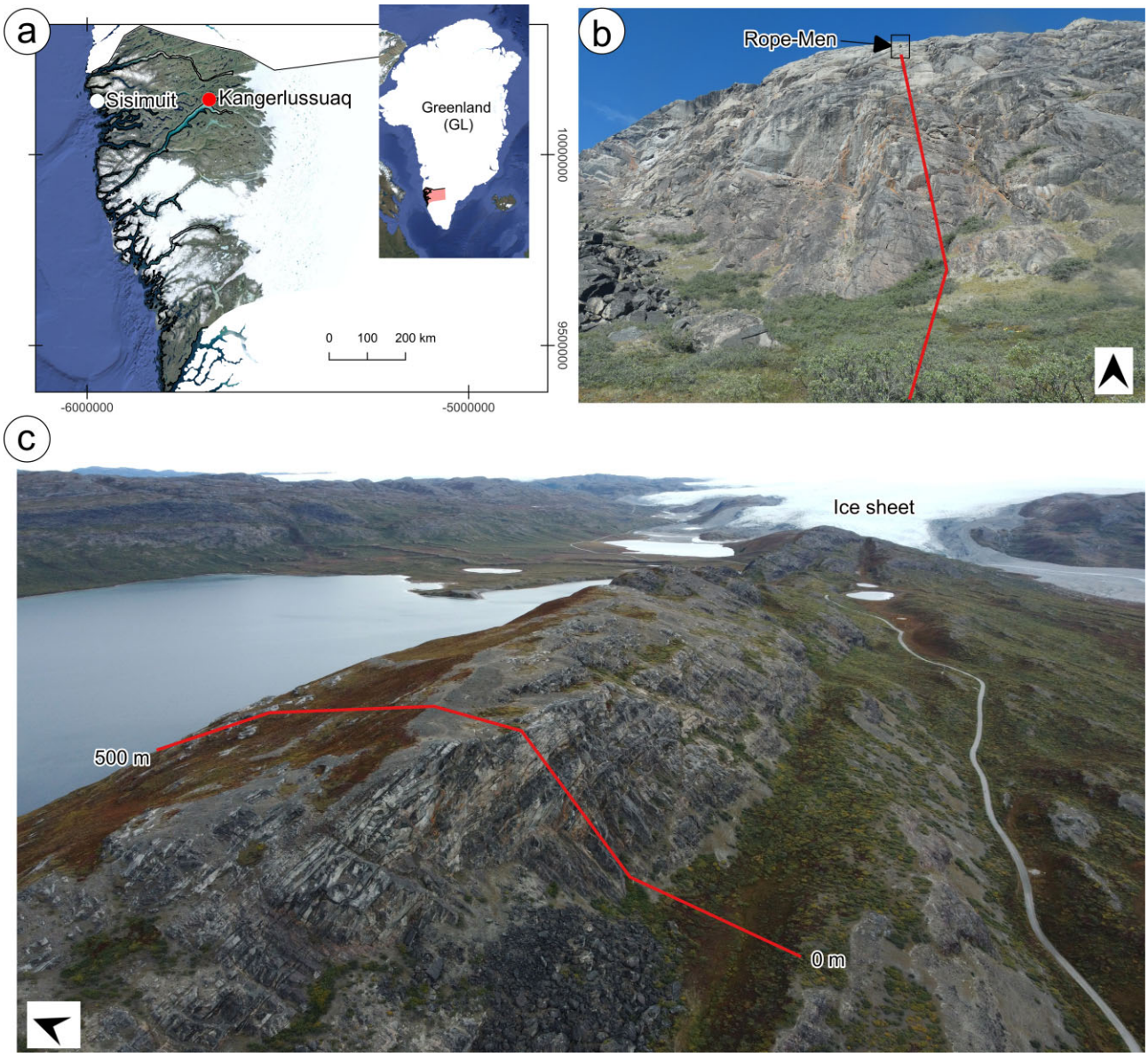

Figure 1. First test site (Site I) corresponding to an East–West orientated granitic ridge located in the Kangerlussuaq mountains of Greenland. (a) Position on the West coast of Greenland. (b) Picture showing the South face and the position of the profile and a rope-men indicate the scale and slope. (c) Picture showing the position of the profile between the South and North face. The beginning of the profile is located on a quartz arenite sand resulting from the disaggregation of the granite, which appears weathered on the South part of the ridge.

2025; Zhou *et al.* 2022; Herring *et al.* 2023; Cathala *et al.* 2024; Fereydooni *et al.* 2024, 2025). Laboratory experiments demonstrate that the presence of ice tends to drastically increase the electrical resistivity of rocks and sediments (e.g. Abu-Hassanein *et al.* 1996; Krautblatter *et al.* 2010). Indeed, during freezing, the pore water (in equilibrium with the mineral paragenesis and therefore relatively conductive (typically ∼100–400 μS cm^{-1} at 25°C) is replaced by ice (a relatively insulating material with conductivity in the range 10^{-7} to 10^{-5} S m^{-1} depending on the frequency, see Revil *et al.* 2025).

In this context, electrical resistivity has been used for several decades as an efficient geophysical tool to image the presence of ice in mountainous and arctic conditions (e.g. Haeberli & Fish 1984; Haeberli *et al.* 2006; Kneisel *et al.* 2008; Mollaret *et al.* 2019; Etzelmüller *et al.* 2020; Zhou *et al.* 2022 and references therein). However, electrical resistivity tomography is notoriously difficult to interpret as a standalone technique because electrical conductivity depends on two contributions, bulk and surface conductivities (Waxman & Smits 1968; Vinegar & Waxman 1984; Revil 2012). At a given temperature, the bulk component of the electrical conductivity is controlled by the liquid water content and the salinity of the liquid pore water while the surface conductivity is controlled by both the liquid water content and the cation exchange capacity (CEC) of the rock (e.g. Waxman & Smits 1968; Vinegar & Waxman 1984; Revil 2012; Duvillard *et al.* 2018). Note that the CEC (usually reported in meq/100 g with 1 cmol kg^{-1} = 1 meq/100 g = 963.20 C kg^{-1}) reflects the number of exchangeable cations on the surface of minerals, especially clay minerals because of their high specific surface area (e.g. Clavier *et al.* 1977; Henry 1997). Note also that crystalline rocks can be very resistive like ice-rich media because of their low porosity and CEC (Piolat *et al.* 2025). This is also the case of strongly desaturated porous media in general.

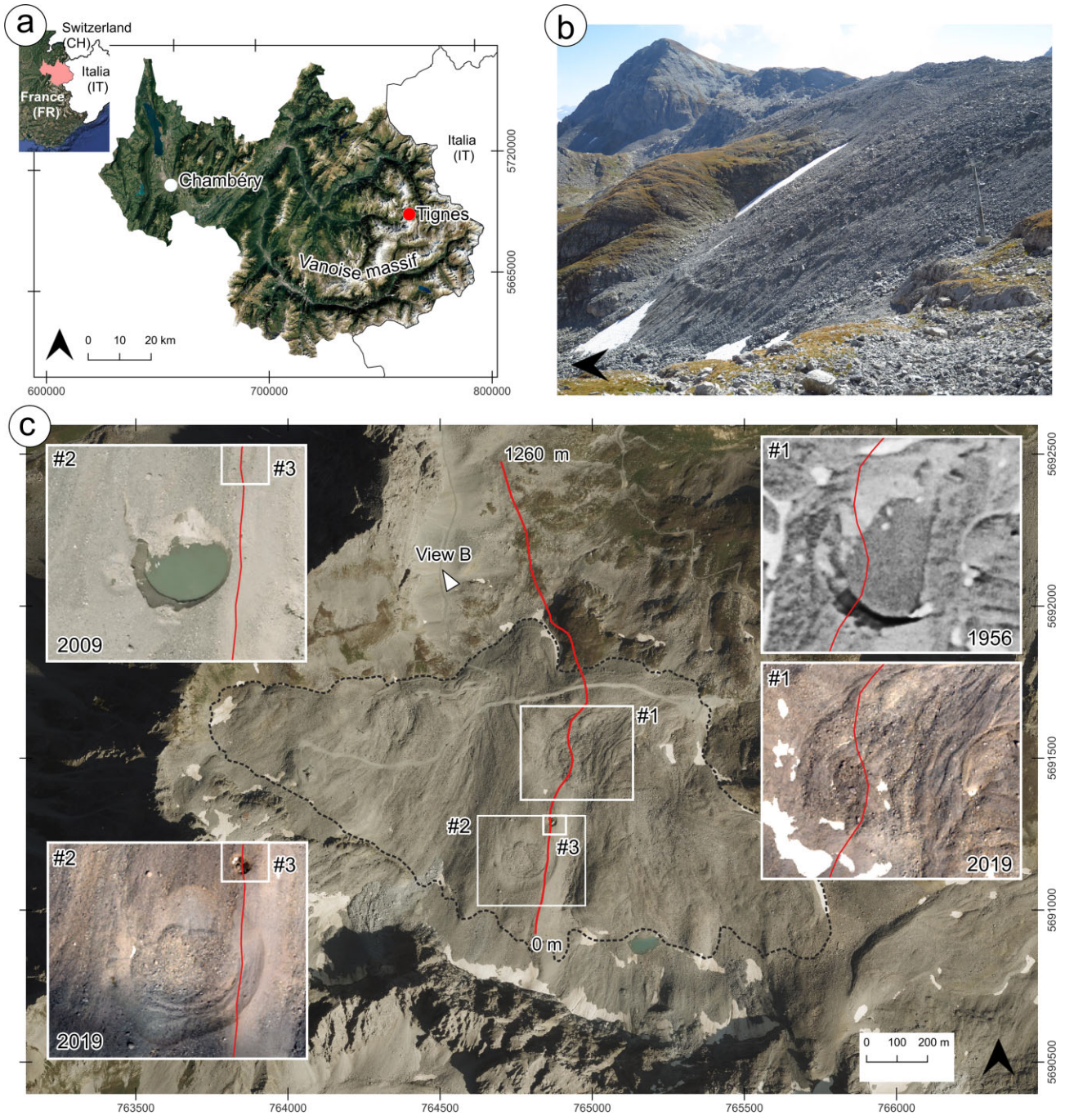

Figure 2. Second test site (Site II) corresponding to a complex ground ice body located in the French Alps. (a) Position in Savoie, France. (b) Picture showing the complex ground ice body. (c) Aerial picture showing the depressions and former lakes in the rock glacier. The roots are in the south part while the front is further North.

Since electrical resistivity depends on two contributions, there is a need for additional methods to separate these two contributions. For instance gamma ray (or spectral gamma ray) is classically used as downhole measurements to quantify the clay content and clay mineralogy and can be used to estimate the CEC (Woodruff *et al.* 2010). In hydrogeophysics, the inability of electrical resistivity to be used as a standalone method has led research scientists to oversimplify the resistivity problem to interpret field data by neglecting surface conductivity (e.g. Herring *et al.* 2019, 2021). This is often done without checking and/or proving the validity of such an assumption (see discussion in Duvillard *et al.* 2018). The same mistake has been done in interpreting electrical resistivity data for volcanoes and geothermal fields for decades while it is now clear that surface conductivity is the dominant conduction mechanism and not the opposite (see for instance Revil *et al.* 2022; Piolat *et al.* 2025, and references therein for a thorough discussion on this topic). The importance of surface conductivity associated with aluminosilicates was clearly demonstrated in the previous paper of this series (Revil *et al.* 2025) and will be demonstrated again below. Not only surface conductivity cannot be neglected but this is the dominant mechanism of electrical conduction in low salinity permafrost environments. This implies that all the works based on (ab)using Archie

Figure 3. Third test site (Site III) corresponding to the Aiguille du Midi (3842 m a.s.l.) in the Mont-Blanc massif (French Alps). (a) Picture showing the NW face with the position of the profile. (b) Picture showing the East face with the position of the profile. The plain lines indicate the approximate position of the geophysical survey. BH-NW indicates the position of the borehole used for the monitoring. (c) Position of the Aiguille du Midi in France. (d) Sketch of the infrastructures showing the galleries and the elevator.

law as a conductivity equation are simply incorrect. Hopefully, there is a solution to this crucial issue as discussed below.

Induced polarization is a complementary geophysical technique to electrical resistivity (e.g. Kemna *et al.* 2002, 2012; Günther *et al.* 2006; Breede *et al.* 2011). It can be measured in the field with the same equipment as used for resistivity measurements but also in the same timeframe. In addition to characterizing the ability of rocks to conduct electricity, induced polarization characterizes their ability to reversibly store electrical charges under an applied electrical field (Olhoeft 1985; Olhoeft & King 1991). This ability is characterized through two interrelated properties named normalized chargeability and quadrature conductivity. The normalized chargeability is a measurement of the dispersion of the (in-phase) electrical conductivity with the frequency (Lesmes & Frye 2001). It is also proportional to the quadrature conductivity measured in frequency–domain measurements as discussed by Revil *et al.* (2017, 2025). The measurement of the normalized chargeability can be used to determine the relative importance of bulk *versus* surface conductivity since the normalized chargeability is proportional to the surface conductivity (Revil 2012, 2013a, b; Weller *et al.* 2013; Coperey et al 2019). In

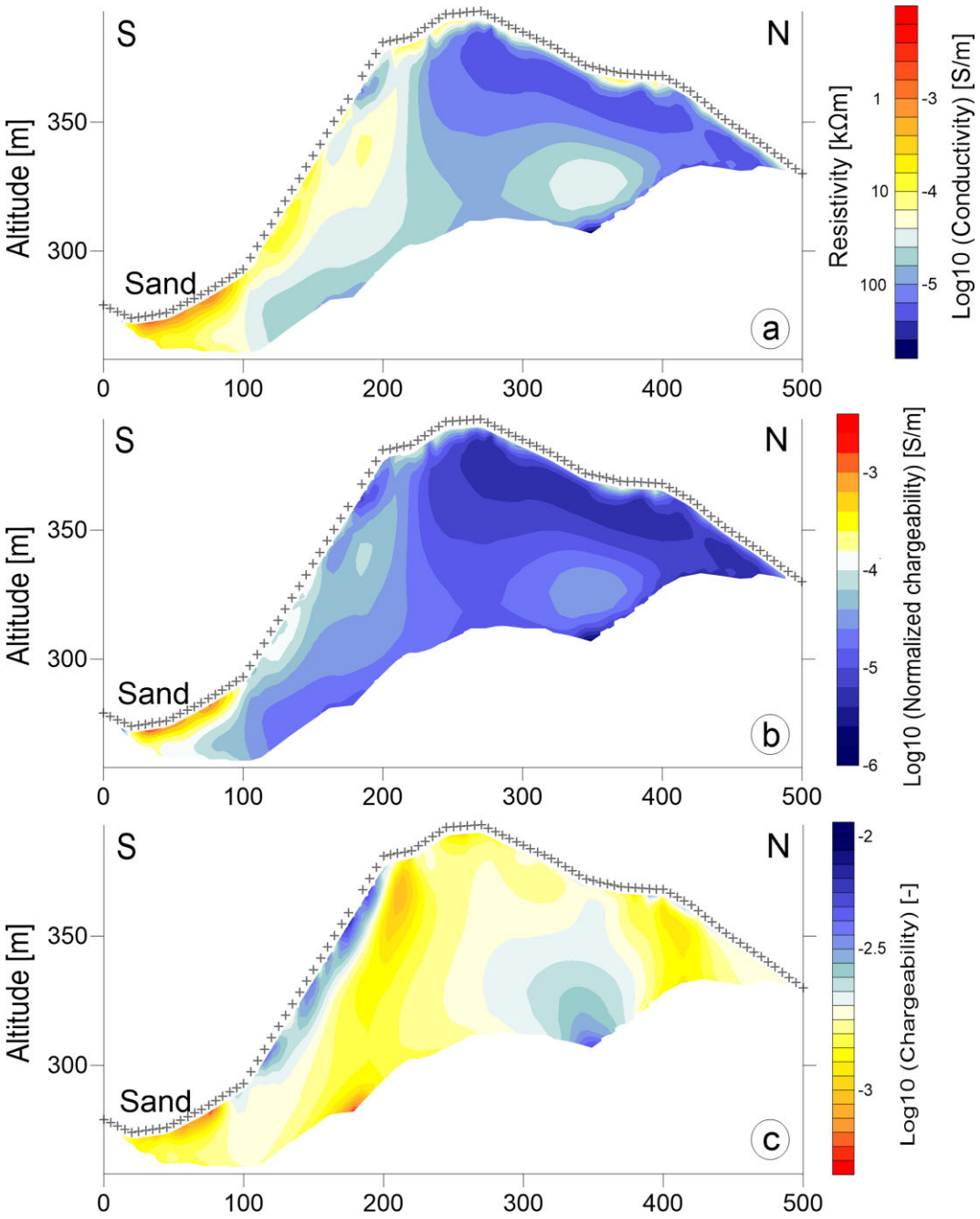

Figure 4. Geophysical tomograms for Site I (Greenland). The crosses along the topography correspond to the position of the electrodes. (a) Electrical conductivity tomogram (expressed in S m^{-1}). (b) Normalized chargeability tomogram (expressed in S m^{-1}). (c) Chargeability tomogram (unitless, note that 1 mV $V^{-1} = 10^{-3}$).

absence of metallic particles, the normalized chargeability and the quadrature conductivity can be connected to the Cation Exchange Capacity (CEC) of a rock, which characterizes the ability of the mineral surface to exchange cations with the pore water. The CEC can be independently determined using titration methods like the cobaltihexamine method (e.g. Orsini & Remy 1976).

While a lot of works has been done with the electrical resistivity method in the context of permafrost (e.g. Petrenko & Whitworth 1999; Vonder Mühll *et al.* 2002; Hauck *et al.* 2004; Hilbich *et al.* 2009; Hauck *et al.* 2011; Mollaret *et al.* 2019; Duvillard *et al.* 2025), investigations using induced polarization remain rather scarce (e.g. Doetsch *et al.* 2015; Duvillard *et al.* 2018, 2021; Abdulsamad *et al.* 2019; Maierhofer *et al.* 2022; Mudler *et al.* 2022; Fereydooni *et al.* 2024, 2025; Moser *et al.* 2025). The development of petrophysical models such as the Dynamic Stern Layer (DSL) model can be used to interpret field data. The Stern layer is the internal part of the electrical double layer coating the surface of mineral grains (Lesmes & Frye 2001) and ice (Daigle 2021). Because of the polarization of the Stern layer, a porous material can reversibly store electrical charges when submitted to a primary electrical field. Other materials behaving like semiconductors (magnetite, pyrite, ice) can also reversibly store electrical charges because of the

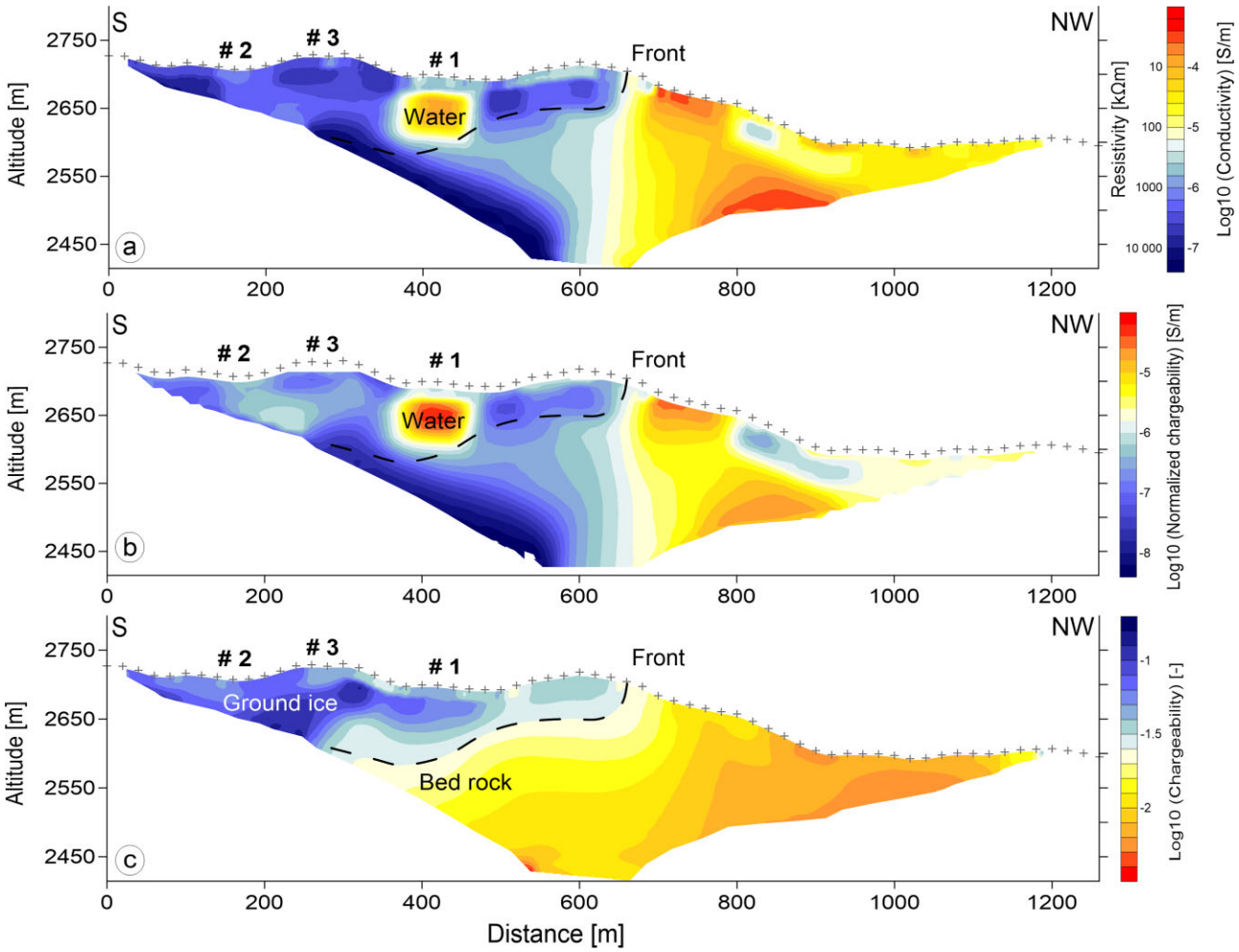

Figure 5. Geophysical tomograms for Site II (Tignes). The crosses along the topography correspond to the position of the electrodes. (a) Electrical conductivity tomogram (expressed in S m^{-1}). (b) Normalized chargeability tomogram (expressed in S m^{-1}). (c) Chargeability tomogram underlying the areas of high ice content (chargeability is unitless but sometimes expressed in mV $V^{-1} \sim 10^{-3}$ in the literature). The positions #1, #2 and #3 refer to three lakes (see Fig. 2).

charge carriers (electrons, protons, p-holes, ionic impurities) they contained.

In the previous paper of this series (Revil *et al.* 2025), the DSL model was completed to account for the polarizability of the ice itself. While semiconductors like pyrite and magnetite are very good conductors at high frequencies (conductivity higher than 100–10 000 S m^{-1}), ice remains a poor conductor at high frequencies. The electrical conductivity of ice has been the subject of numerous works including the frequency-dependence of its surface conductivity (Caranti & Illingworth 1983). The role of ice has been discussed and modelled in the first paper of this series and has been the subject of numerous works in physics and geophysics (e.g. Petrenko & Ryzhkin 1997). If liquid water is present in the porous material and because of the high resistivity of the ice crystals, the electrical current is expected to flow in the liquid pore water as long as it is connected above a percolation threshold. Therefore it would not polarize the bulk volume of the ice crystals. That said, ice is a curious semiconductors because protons can also move along its surface and create a polarization at the scale of the ice crystals or aggregates. In the previous paper of this series (Revil *et al*. 2018), we have demonstrated that this interfacial polarization can be represented by an equivalent bulk surface conductivity and polarization with a chargeability that depends on the volumetric ice content. At the opposite, in the case of dry ice, we expect to see the polarization mechanisms discussed by Stillman and co-workers (Stillman *et al.* 2010, 2013a, b, 2018; Grimm *et al.* 2015) because, precisely in this case and in this case only, the electrical current is forced to move through the ice crystals.

We first present below the results of three geophysical surveys using time-domain induced polarization at three sites characterized by the presence of permafrost. One is located in Greenland and two are located in the French Alps. Then, we use the updated DSL petrophysical model developed in the previous paper of this series to interpret these three field surveys in the context of ground ice conditions. The three field sites have been selected because they complement each other. Indeed, two of them correspond to low-porosity crystalline rocks (granite and granodiorite) and the last one corresponds to a highly porous rocks in a rock glacier (ice mixed with rock debris).

Site I is located in Greenland close to Kangerlussuaq. It corresponds to an East–West elongated ridge (392 masl, metres above sea level) that is partially altered and frozen in its North face (Fig. 1). The granodiorite present at this site is an old granitoid that is partially weathered. The second site is located close to Col des Vés (2846 m a.s.l.) in the Vanoise massif (France). At this site, we observe a massive ground ice body overlying a low-porosity marble

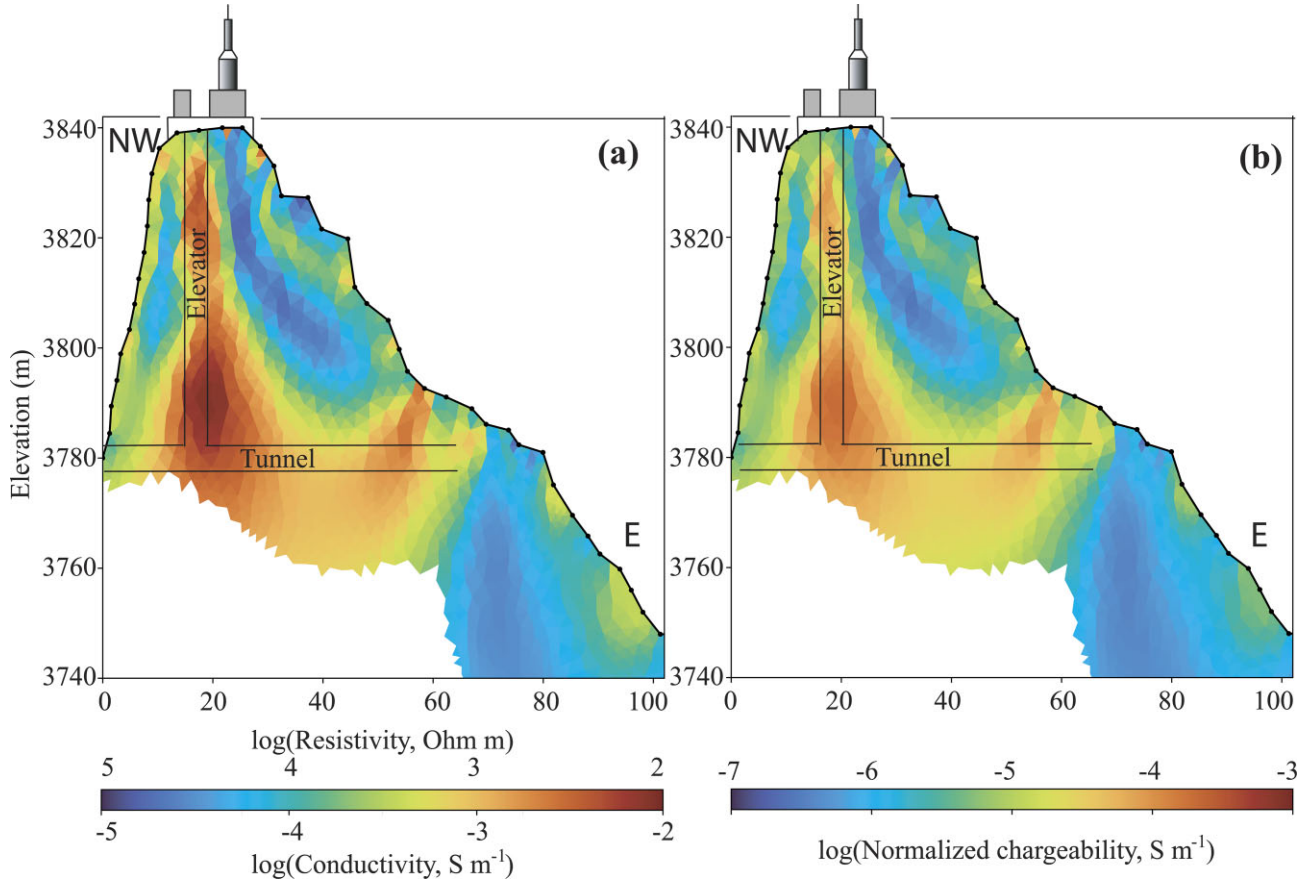

Figure 6. Geophysical tomograms for Site III (Aiguille du Midi, France). The black circles along the topography correspond to the position of the electrodes. (a) Electrical conductivity tomogram (expressed in S m^{-1}). (b) Normalized chargeability tomogram (expressed in S m^{-1}).

substratum. In this case, the ice is probably wet, which means that the ice crystals still remains coated with a film of liquid water implying a strong role for the frequency-dependent surface conductivity of ice. This periglacial system displays a remarkable variation in the ice content. The roots are formed by nearly pure ice covered overlaid by a thin debris cover (Fig. 2). Site III corresponds to a profile along the Aiguille du Midi (3842 m a.s.l.) in the Mont-Blanc massif (France, Fig. 3). The rock is formed by a relatively fresh granite fractured in some areas.

2 TEST SITES AND SURVEYS

2.1. Background and geophysical surveys

The first test site (labelled Site I hereinafter) is located near the settlement of Kangerlussuaq, in the Qeqqata municipality in the Central Western Greenland and about 8 km from the current Greenland ice sheet (Fig. 1). This site has been chosen because the lithology corresponds to a Precambrian granodiorite characterized by some degree of alteration because of its age. The geomorphological context is characteristic of a so-called '*roches moutonnées*' landscape, with depressions as observed at the base of the southern face of the investigated area (see Fig. 1). These depressions are filled with sandy till deposits resulting from the past glacial extension of the Greenland ice sheet and the degradation of the altered granodioritic side of the ridge. In the Kangerlussuaq region, permafrost distribution is primarily determined by elevation and slope aspect. Snow cover does not show significant influence (Marcer *et al*. in press). Permafrost is present at all elevations on the north-facing slopes, while it is generally absent or fading on south-facing slopes at lower elevations (below 394 m.a.s.l.), suggesting increased sensitivity to recent climate warming (Marcer *et al*. in press).

The geophysical field survey was conducted in August 2021 using a 400-m-long cable with 80 electrodes spaced at 5-m intervals. Two measurement cables were installed on the south face (one following the other), requiring ropes for setting up the survey in the vicinity of the top part of the ridge. A roll-along technique with a 100-m electrode shift was used to extend the profile in the North direction. Both electrical conductivity and chargeability measurements were performed. The survey parameters are the following: (1) squared current injection with a period $T = 1$ s, (2) 10 windows of 0.1 s to measure the secondary voltage curve and (3) dead time of 0.1 s after stopping the primary current injection.

The second site (Site II) is located on the East side of Col des Vés (Vanoise massif, Western European Alps, ∼2750 m a.s.l., France). This site corresponds to a debris-covered glacier in its upper part, followed by a rock glacier characterized by the presence of thermokarsts and lakes on its surface (Fig. 2). Three generations of lakes have been observed since 1950, with varying degrees of spatial extent. The local climatic conditions are favourable to the presence of permafrost, while permafrost is potentially thawing in the central area and along its lateral boundaries (Marcer *et al.* 2017, 2019, 2024). The geophysical data were acquired in August 2019 along a 1260-m-long cable (20-m spacing between the electrodes, 64 electrodes). The same acquisition parameters were used than in the Greenland survey.

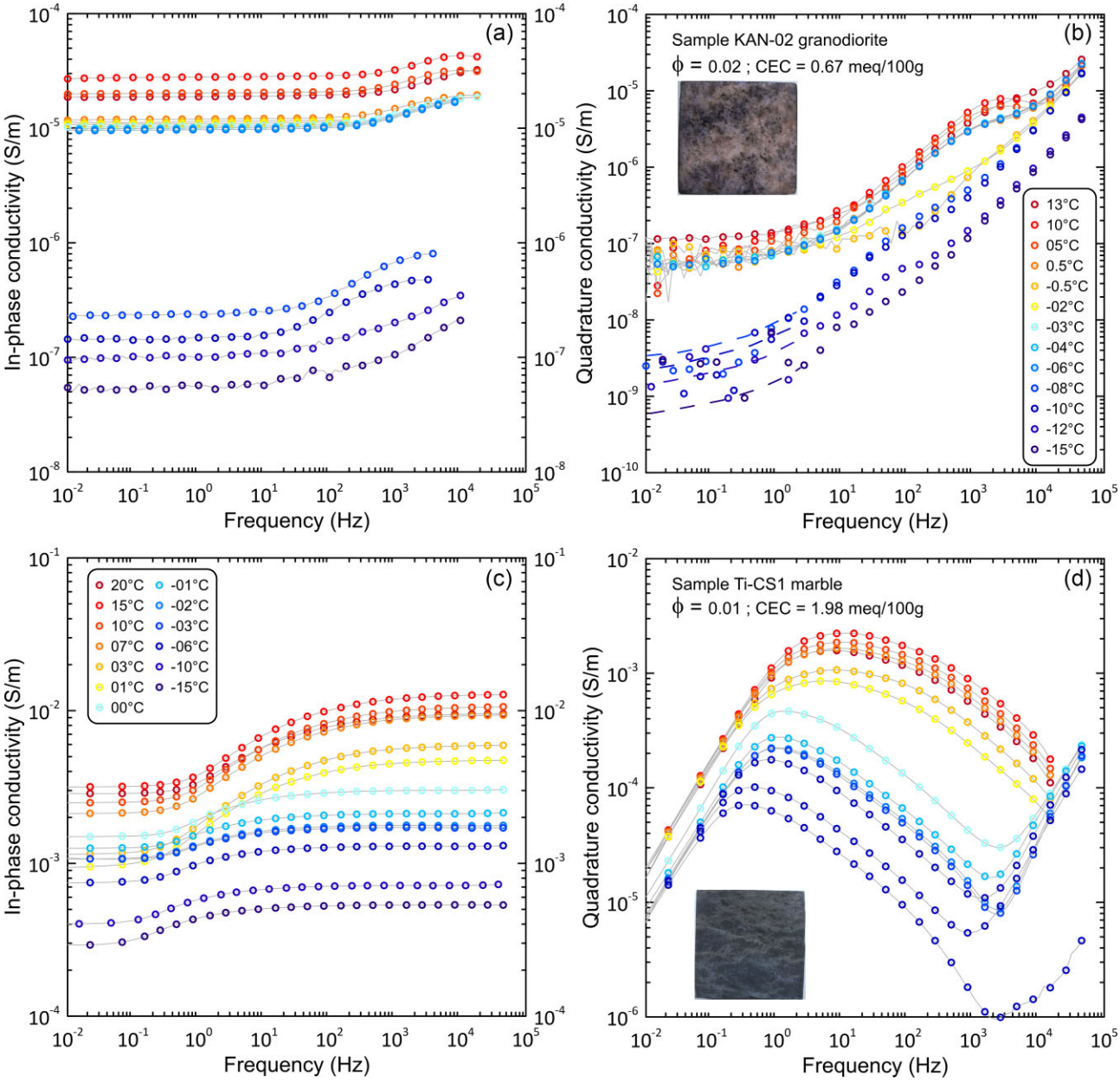

Figure 7. Complex conductivity measurements for two rock samples from Sites I (granite) and II (marble, basement, see Table 1 for their properties). (a) In-phase electrical conductivity spectrum of rock sample of KAN-02 granodiorite from Site I (Sisimiut, Greenland). (b) Quadrature conductivity spectrum of rock sample of KAN-02 granodiorite from Site I (Sisimiut, Greenland). (c) In-phase electrical conductivity spectrum of rock sample of Ti-CS1 Marble from Site II (Tignes, France). (d) Quadrature conductivity spectrum of rock sample of Ti-CS1 Marble from Site II (Tignes, France). The size of the cubic samples is 3 cm. Pore water conductivity 100 μS cm^{-1} at 25°C.

The third survey (Site III) concerns the Aiguille du Midi (3842 m a.s.l.), which is located in the Mont-Blanc massif (French Alps). The investigated site is located on the north–west flank of the massif (Fig. 3). It includes three peaks interconnected by artificial bridges and galleries. Our survey focuses on the central peak, which is the highest among the three. The Aiguille du Midi hosts a cable car station at nearly 4000 masl (Fig. 3). Its construction started in the early 1950s. The lithology corresponds to fresh and compact granite (310 ± 10 Myr; Leloup *et al.* 2005) characterized by very low porosities (∼ 0.01, Magnin *et al.* 2015a) but heavily fractured and permeable in some areas. That said, the highest parts (3740 to 3840 m a.s.l.) of the peak contain few large fractures (Magnin *et al.* 2015b). The acquisition parameters used in our survey, performed in September 2019, are the following: (1) period for the current injection 0.5 s., (2) deadtime 0.1 s and (3) the voltage decay was recorded on ten windows of 0.1 s. We focus on the first recording window between 0.1 and 0.2 s after shutting down the current between the AB electrodes. Indeed, as a rule of thumb, the considered windows should be the first windows that can be considered as electromagnetic noise-free with the two times of the windows much shorter than the characteristic decay time of the secondary voltage. The survey comprises 43 electrodes with a spacing of 5 m.

In the two first field surveys, we use 64 10-mm-thick and 40 cm-long stainless-steel electrodes and at the Aiguille du Midi we use

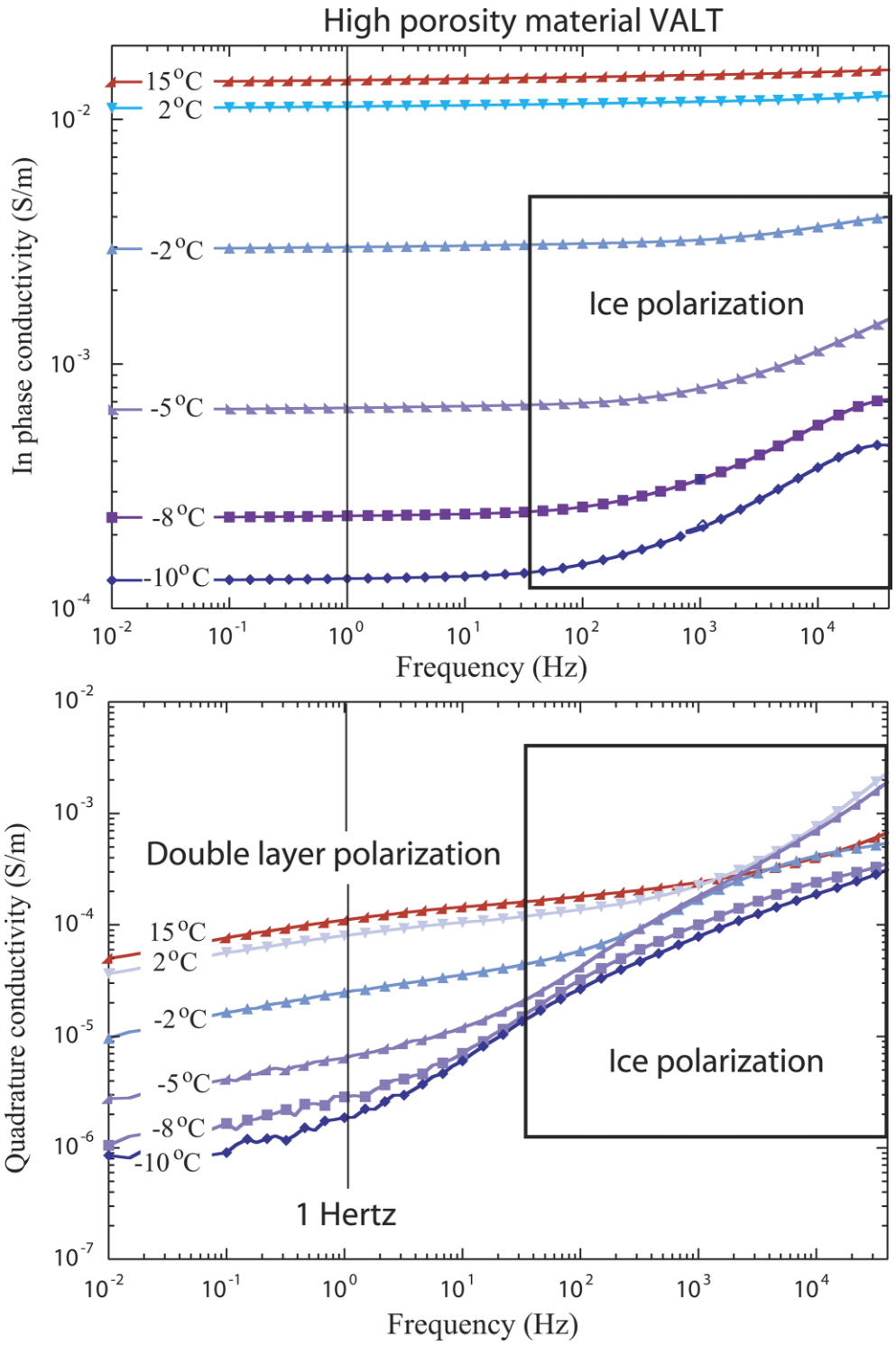

Figure 8. Complex conductivity spectra for the soil sample (VALT, see Table 1) during freeze. We plot the in-phase and quadrature components of the complex conductivity *versus* the frequency of the input current. Note that there is a new dispersion phenomenon that starts to appear under freezing conditions, possibly associated with the polarization of ionic and Bjerrum defects in the ice itself and especially on the surface of the ice crystals. This polarization is superposed to the Maxwell–Wagner polarization mechanism. The lines are just guides to the eyes. Pore water conductivity 100 μS cm^{-1} at 25°C (snowmelt in equilibrium with the minerals). Modified from Duvillard *et al.* (2018).

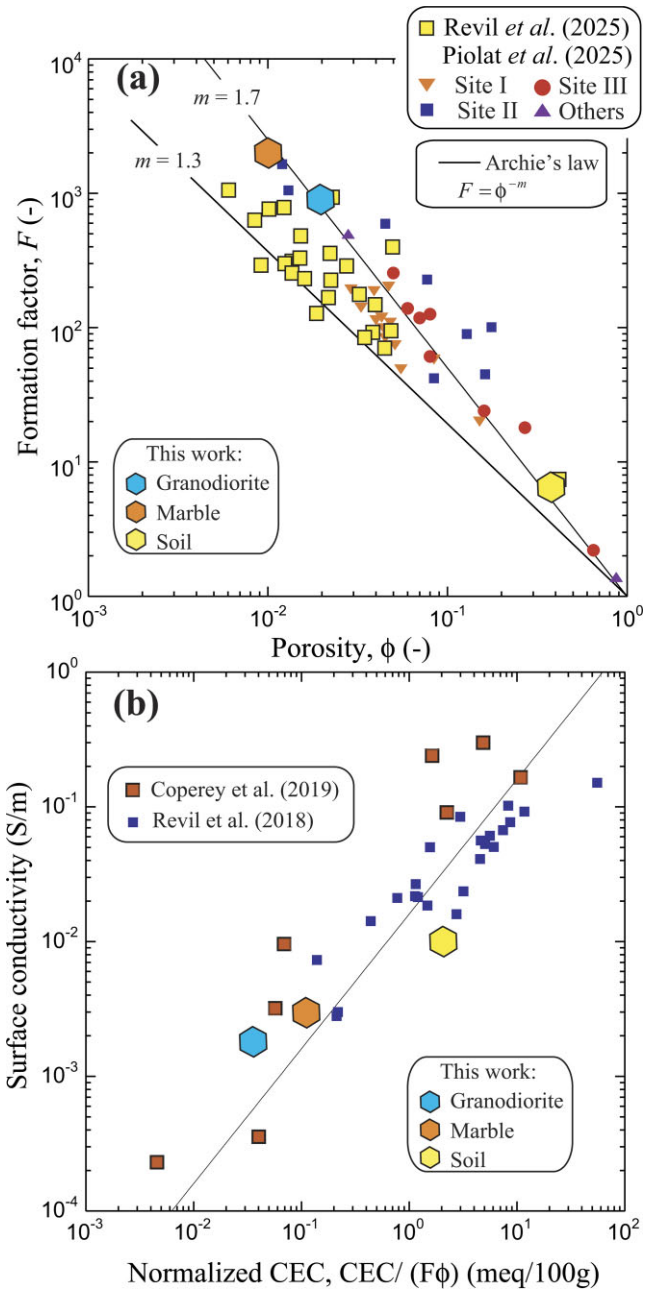

Figure 9. Influence of the porosity and CEC on the formation factor and surface conductivity. (a) Formation factor versus porosity. Comparison between the data obtained in this paper and those obtained in two other studies. The plain lines correspond to Archie's law with two distinct values of the cementation exponent m. (b) Surface conductivity versus the normalized CEC (CEC divided by the tortuosity of the bulk pore space defined as the product of the formation factor by the porosity).

stainless steel expansion bolts with a length of 10 cm as electrodes. The induced polarization data were acquired with an ABEM/SAS-4000 resistivity metre. Salted water and bentonite mixtures were used to improve the electrical contacts between the electrodes and the ground (e.g. Maurer & Hauck 2007). The position of the electrodes was taken with a differential GPS (Global Positioning System) with a precision of ∼10 cm.

2.2. Results

The inversion of the apparent resistivity and apparent chargeability data is done with the RES2DINV software (Loke 2002) for Sites I and II and pyGIMLI (open source package, see Rücker *et al.* 2017) for site III. We used pyGIMLI for Site III because of its extremely strong topography, which cannot be handled by RES2DINV. Since the two codes are based on a very similar inversion strategy (despite some differences in the way measurement errors are handled or how smoothness constraints are applied), we obtain code independent results as tested on simple synthetic cases. In the three cases, the cost function is indeed minimized penalizing the roughness of the tomograms. For Sites I and II, convergence was reached in five iterations for the apparent resistivity data and five iterations for the apparent chargeability data. For Site III, convergence was reached in five iterations for the apparent resistivity data and only three iterations were needed to invert the apparent chargeability data. The results of the tomograms are displayed in terms of inverted conductivity or resistivity, normalized chargeability and chargeability tomograms in Figs 4 and 5 for Site I and II, respectively, and in Fig. 6 for Site III.

For Site I (Greenland), the conductivity and normalized chargeability vary over three orders of magnitudes (10^{-2} to 10^{-5} S m^{-1} for the conductivity, 10^{-3} to 10^{-6} S m^{-1} for the normalized chargeability) while the chargeability varies over one orders of magnitude (10 to 1 mV V^{-1} with 1 mV V^{-1} $= 10^{-3}$). The sand at the beginning of the profile is characterized by high values of the conductivity and normalized chargeability. The South flank of the ridge (altered) is characterized by a high conductivity and intermediate values for the normalized chargeability. The North flank (which is frozen) is characterized by very low values of the conductivity and normalized chargeabilities). The frozen rock does not show up a specific signature on the chargeability tomogram.

For Site II (Tignes, France), the conductivity and normalized chargeability vary over three orders of magnitudes (10^{-3} to 10^{-7} S m^{-1} for the conductivity, 10^{-4} to 10^{-8} S m^{-1} for the normalized chargeability) while the chargeability varies over one orders of magnitude (200 to 1 mV V^{-1} with 1 mV V^{-1} $= 10^{-3}$). The rock glacier is characterized by low values of the conductivity and normalized chargeability with little contrast with the substratum (compact marble). The very conductivity is consistent with the resistivity data (over 1 MOhm m, ice content 35 to 60 per cent) obtained recently by Zhou *et al.* (2022) in the Tianshan mountains of China. The rock glacier is characterized by very high values on the chargeability tomogram (>100 mV V^{-1}), which is in contrast with the marble itself. The area downstream of the rock glacier is characterized by high values of the conductivity and normalized chargeability and low values of the chargeability. In the next section, we describe laboratory experiments with the goal to decipher the previous field responses in quantitative terms thanks to the updated DSL model.

For Site III, the electrical conductivity varies in the range 10^{-5} to 10^{-2} S m^{-1} while the normalized chargeability is in the range 10^{-3} to 10^{-7} S m^{-1} (Fig. 6). This range is similar to the range observed for Site I corresponding to the granite in Greenland (see Fig. 4). Fig. 6 exhibits a vertical conduit in the central part of main peak of Aiguille du Midi that may be associated to the presence of the elevator that is used to access to the upper platform with the antenna (Fig. 3). The presence of the galleries and elevator contributes to heating the granitic peak from inside increasing both the conductivity and the normalized chargeability above the freezing temperature. A direct effect of the presence of metallic infrastructure (e.g. armed concrete) is possible but not clearly observed. This may be due to the small

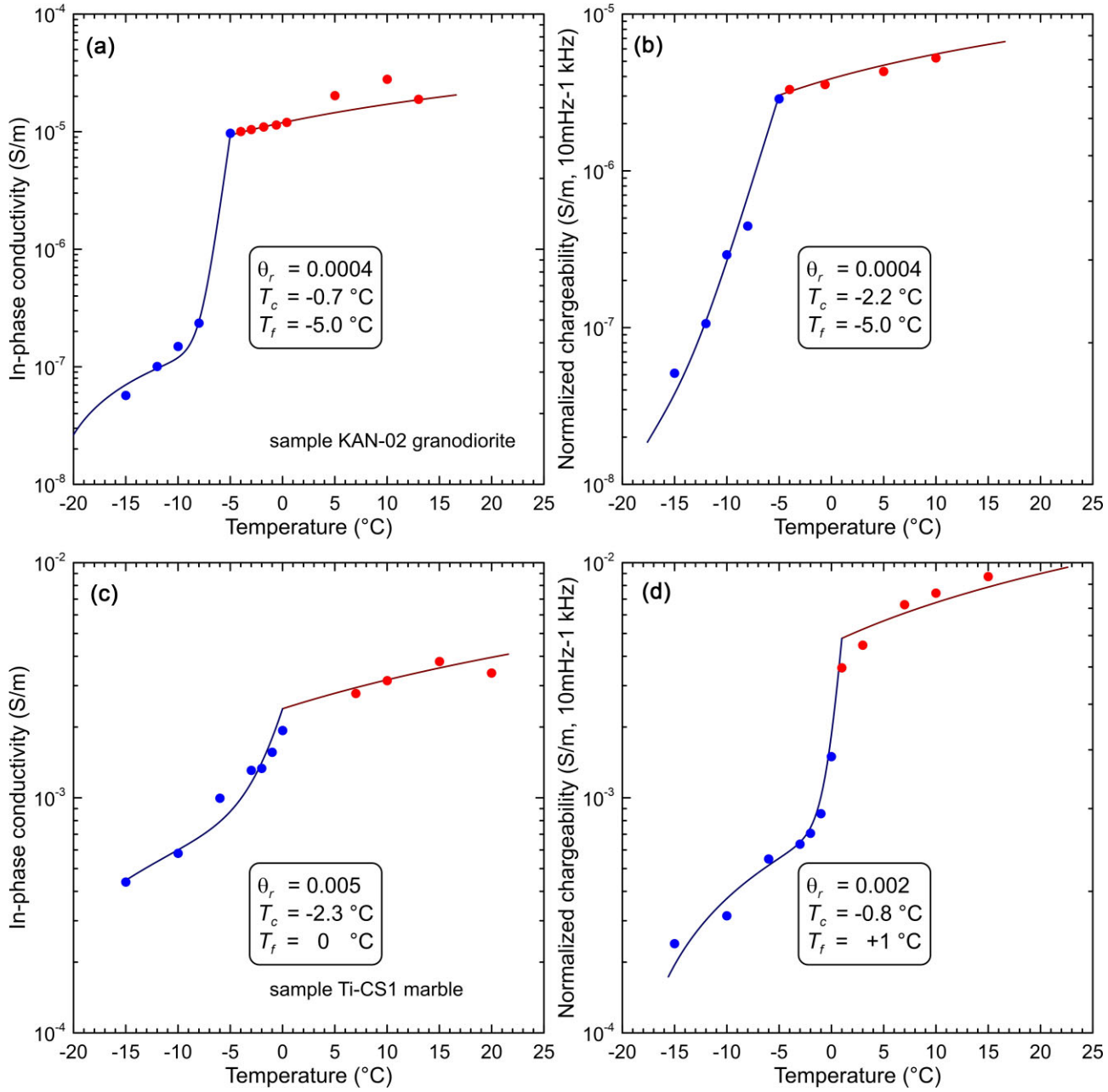

Figure 10. Influence of the temperature on the conductivity and normalized chargeability of the two crystalline rocks investigated in this study. (a) Electrical conductivity. Sample KAN02 (graniodiorite). (b) Normalized chargeability. Sample KAN02 (graniodiorite). (c) Electrical conductivity. Sample Ti-CS1 (marble). (d) Normalized chargeability. Sample Ti-CS1 (marble).

volume fraction of metals with respect to the size of the investigated domain. We will come back to the interpretation of the field data in Section 4 below.

3 LABORATORY EXPERIMENTS

We selected two low-porosity core samples from the test sites to see the effect of temperature on their complex conductivity spectra. In addition, we use a third high porosity sample from the study of Duvillard *et al.* (2018) to see the effect of high porosity and therefore high ice content at low temperatures. The two low-porosity samples correspond to a granodiorite sample (KAN-02) from the ridge shown in Fig. 1 (Site I) and a marble sample (Ti-CS1) from the substratum of Site II (Fig. 2). The experimental data are shown here and not in Revil *et al.* (2018) because of their relevance to the field data explored in this paper. The samples were first dried at 60°C for 2 d. Then there were saturated under vacuum (1 mbar) with a degassed pore water conductivity corresponding to melted snow. After saturation, we waited for four weeks before proceeding to the complex conductivity measurements to be sure that the pore space was fully saturated. We followed the same experimental procedure as in Coperey *et al.* (2019). The complex conductivity measurements were performed thanks to the impedance spectrometer developed by Zimmermann *et al.* (2008). This spectrometer is

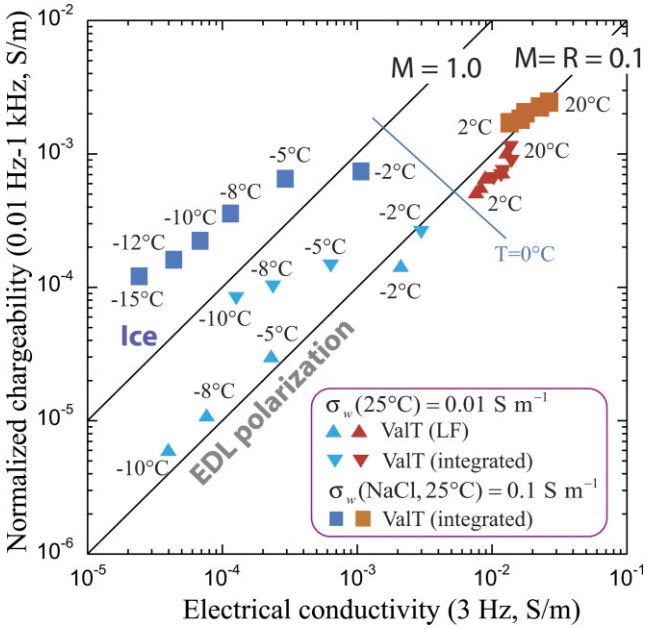

Figure 11. Relationship between the normalized chargeability and the electrical conductivity including and excluding the direct contribution of ice. Both at very low salinity (100 μS cm^{-1}, 25°C, snowmelt) and higher salinity (1000 μS cm^{-1}, 25°C, NaCl solution), we see that above the freezing temperature, the data conforms to the prediction of the DSL model in absence of semiconductors and when surface conductivity dominates the overall conductivity response (in this case the ration of the normalized chargeability by the conductivity is equal to $R = 0.10$). Below the freezing point, the integration of the spectra from low-to-high frequencies (0.01 Hz–1 kHz) displays a very strong polarization associated with the direct effect of ice acting as a protonic semiconductor. The presence of salt (NaCl) increases this polarization because of ionic impurities boosting both the dielectric response of the material and its semiconductor properties. LF: Low frequency (10^{-2}–1 Hz). EDL: Electrical double layer.

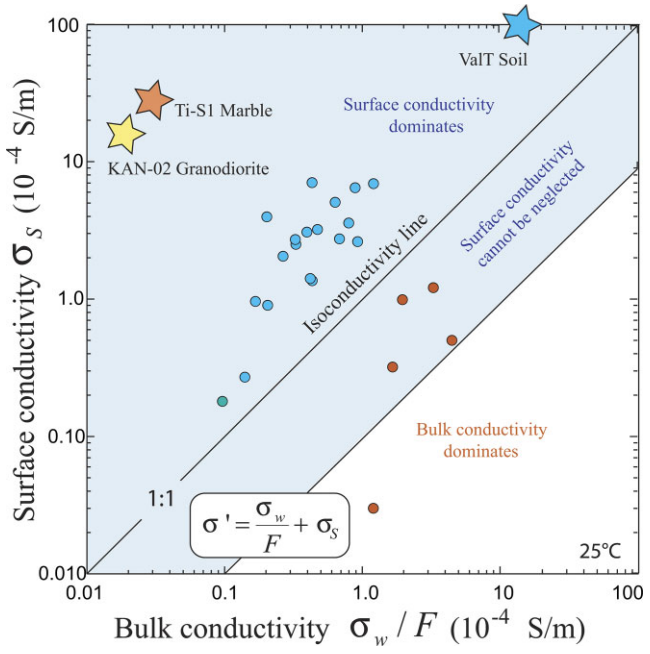

Figure 12. Comparison between surface and bulk component of the conductivity. The data indicates that for snowmelt used to saturate the samples, the surface conductivity dominates the conductivity of the material for the three samples analysed in this study. The blue area (in which nearly all the data points are located) corresponds to the area for which Archie's law taken as a conductivity would grossly fail to work.

Table 1. Properties of the rock samples. The CEC denotes the cation exchange capacity (1 cmol kg^{-1} = 1 meq/100 g = 963.20 C kg^{-1}), F the (intrinsic) formation factor and σ_S the surface conductivity.

Sample	KAN-02	Ti-CS1	ValT
Lithology	Granodiorite	Marble	Soil
Porosity ϕ (-)	0.02	0.01	0.38
CEC (meq/100 g)	0.67	1.98	5.30
F (-)	933	1801	6.7
σ_S (10^{-4} S m^{-1})σ_w(μS cm^{-1})	18100	30100	100100

based on the four-point measurement method and offers a measurement range from 1 mHz to 45 kHz with an accuracy better than 0.1 mrad in most of this frequency range.

The complex conductivity spectra are shown in Fig.7 The two samples correspond to low-porosity materials, but, that said, their spectra are vastly different. The transition from unfrozen to frozen is very abrupt for the granodiorite sample and smoother for the marble sample. Also, we clearly see a peak in the quadrature conductivity data for the marble sample that moves to lower frequencies when the temperature decreases. Since both samples are characterized by very low porosities, it is expected from the first paper of this series (Revil *et al.* 2025) that we should not see direct evidence for ice polarization. This is indeed the case since no direct polarization effects is visible when temperature decreases. The effect of the freezing arises because of a change in the liquid water saturation in the pore space of the material and concomitant increase of the salinity in the liquid pore water.

In order to compare these data with a high porosity material underlying freezing, we use the data reported by Duvillard *et al.* (2018) for a high porosity soil (its complex conductivity spectra are shown in Fig. 8). In this case, a new dispersion phenomenon starts to emerge under freezing conditions with the decrease of the temperature. This polarization is likely associated with the polarization of ionic and Bjerrum defects on the surface of the ice crystals as described in details by Revil *et al.* (2025). We will come back on this polarization mechanism a bit further below. But first we check that our data on the three porous materials conforms to Archie's law for the relationship between the (intrinsic) formation factor F and the porosity ϕ, and between the surface conductivity σ_S and the ratio between the CEC and the tortuosity of the bulk pore space defined as the product of the formation factor and the porosity of the material. We recall here that the (in-phase) conductivity is related to the formation factor F by,

$$\sigma'(\omega) = \frac{1}{F}\sigma_w + \sigma_S'(\omega), \tag{1}$$

where $\sigma_S'(\omega)$ denotes the in-phase surface conductivity and σ_w is the pore water conductivity. Eq. (1) makes clear that the formation factor is not equal to the resistivity of the material divided by the resistivity of the pore water (as erroneously written in many papers). The results show in Fig. 9(a) confirms the choice for the value of the cementation exponent $m = 1.5 \pm 0.3$. Fig. 9(b) provides the value of the product between the mass density of the grains ρ_g (2700 kg m^{-3} for silicates and aluminosilicates) and 2900 kg m^{-3} for carbonates) and the effective mobility B at 25°C. The temperature dependence of B is described in the first paper of this series (Revil *et al.* 2025)

Fig. 10 shows the effect of the temperature on the conductivity and normalized chargeability data for the two crystalline rock samples. The curves describing the effect of the temperature below the freezing point is well captured by the exponential freezing curve developed in Duvillard *et al.* (2018). This curve can be associated in turn to the pore size distribution (Luo *et al.* 2023,

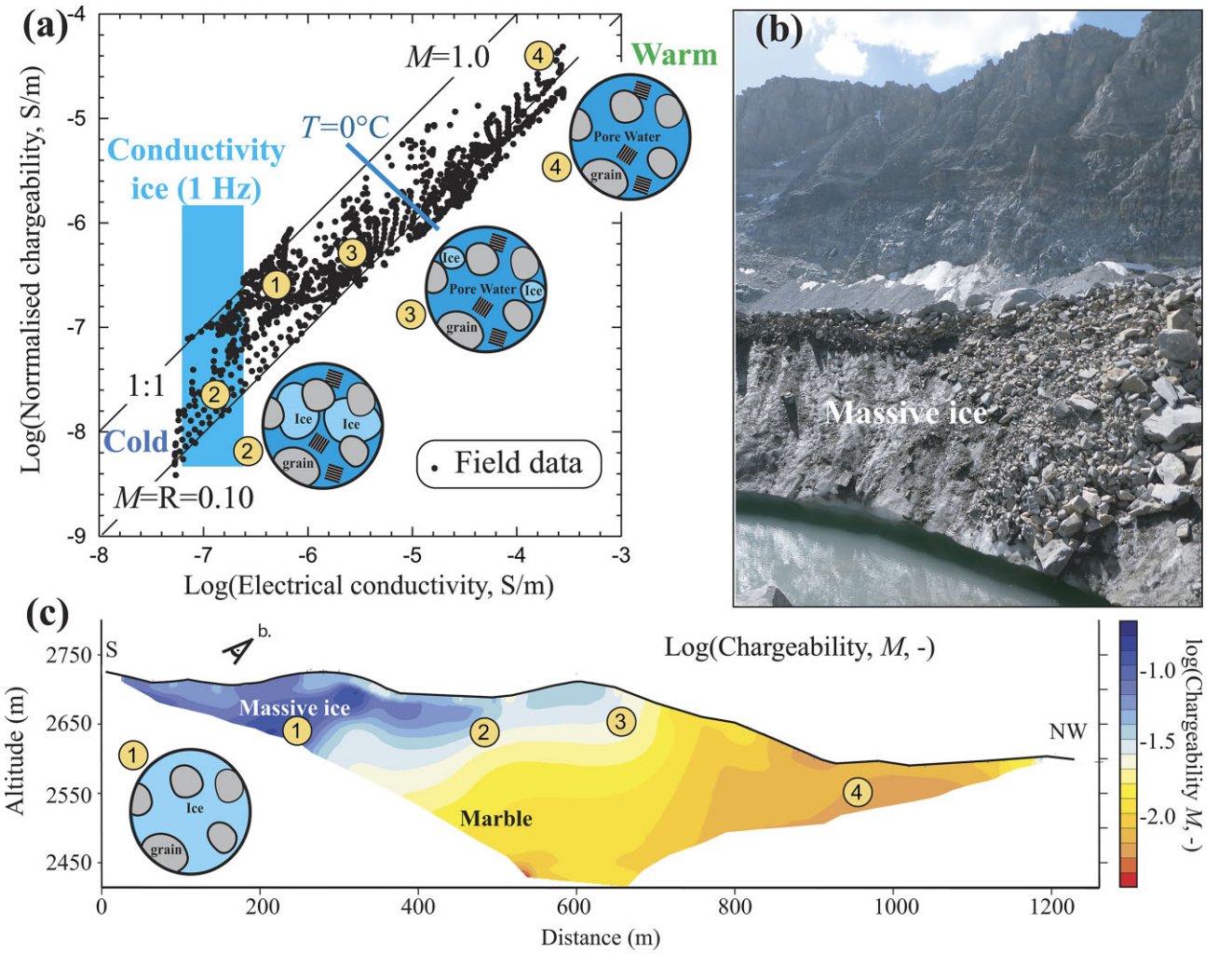

Figure 13. Analysis of the ice content at the Col des Vés rock glacier (Site II). (a) Normalized chargeability *versus* electrical conductivity. The transition between massive ice to permafrost with a decreasing level of ice is clearly visible on this plot. At −10°C, the conductivity of ice at 1 Hertz is 5×10^6 Ohm m. (b) Picture showing the presence of massive ice in the upper part of the ground ice body. (c) Interpretation of the chargeability tomogram in terms of massive ice. This showcases the role of ice in the chargeability data because ice is a dirty protonic semiconductor. The low-porosity substratum (made of marble) does not exhibit such a property and if permafrost is present, its volumetric ice content remains small.

2024a, b, 2025). Above the freezing temperature, the conductivity and normalized chargeability data depends weakly on temperature. The texture (formation factor) and CEC control the conductivity and normalized chargeability values above the freezing temperature while the temperature has a drastic effect below the freezing temperature. Because of the change of slope in the trends above and below the freezing temperature, we may expect a minimum in the distribution of the conductivity and normalized chargeability data in the observed field tomograms (see discussion in Duvillard *et al.* 2021). We will check this prediction in the next section.

In Figs 8 and 11, we focus on the complex conductivity data of the soil sample #ValT since it presents a high porosity ($\phi = 0.38$) susceptible to show the direct and indirect effect associated with the presence of ice. If we use the data set with snowmelt (100 μS cm^{-1} at equilibrium with the sample, 25°C), the plot between the normalized chargeability and the conductivity conforms to the model prediction when (i) surface conductivity dominates the overall response of the material and (ii) if we use the low frequency data (the normalized chargeability is here the normalized chargeability determined over two decades times 0.01–1 Hz, a correction factor of 3 if applied to simulate the normalized chargeability over the full spectrum using the constant phase model approach developed by Revil *et al.* 2017). In this case, the data are not 'contaminated' by the direct effect of ice polarization which starts to develop at frequencies above 1 Hz. Instead, if we use the normalized chargeability integrated over the spectrum (0.01 Hz–10 kHz), the situation is very different below the freezing point (Fig. 11). We clearly see a very strong polarization effect which tends to lead to a chargeability M close to 1 when the ice content is becoming important (see Revil *et al.* 2025). Here again, as explained in the first paper (Revil *et al.* 2018), ice polarization is coming from its surface properties: it polarizes along its surface because of the presence of protons and not because of its bulk properties. In presence of liquid water coating the surface of the ice crystals, the electrical current will flow outside the ice crystals, along their surface, but not through their bulk components. This is a major difference between our approach and previous models.

Even more intriguing is the case when we use a high conductivity electrolyte as pore water. For instance, we also show in Fig. 11, the case when the same soil (ValT) is saturated by a NaCl salt solution at 0.1 S m^{-1} (1000 μS cm^{-1} at 25°C). The result above the freezing

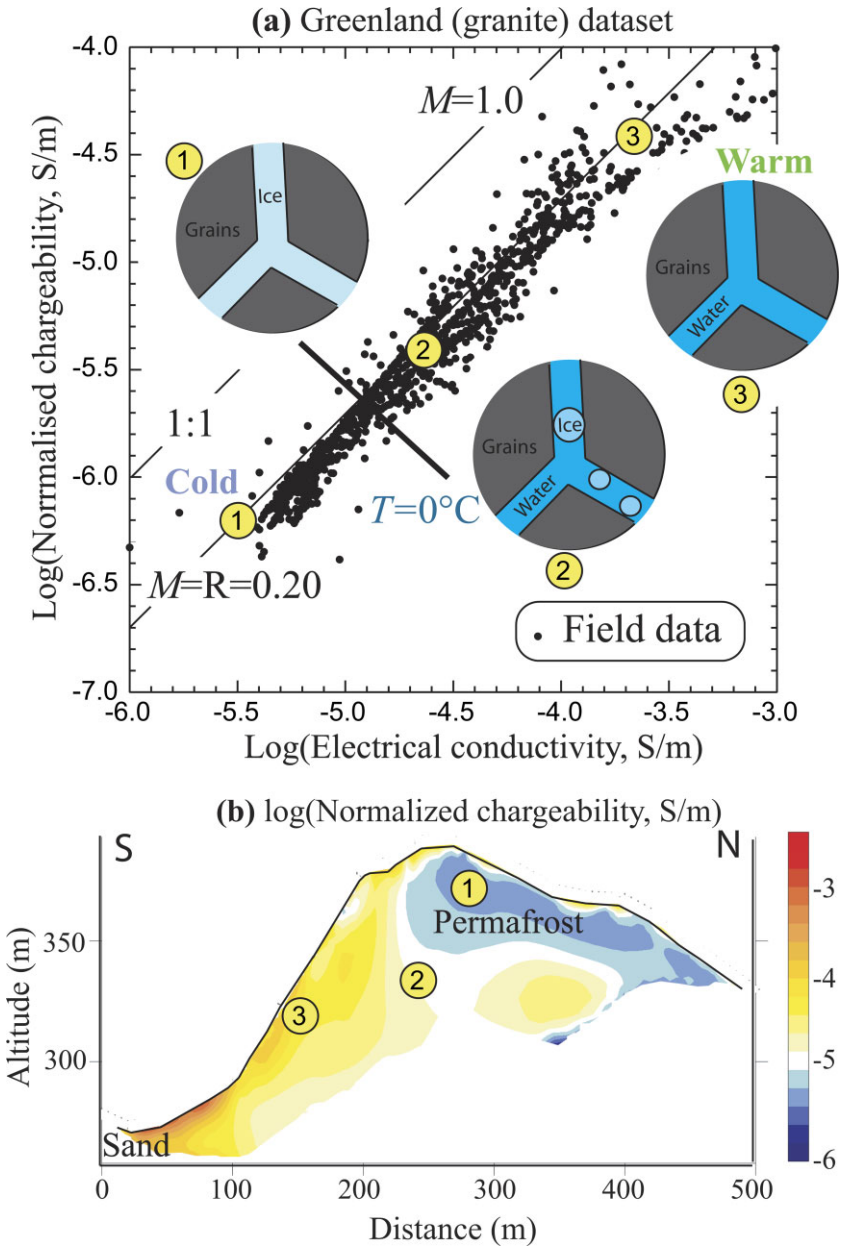

Figure 14. Site I (Greenland). (a) Normalized chargeability *versus* electrical conductivity. The transition between ice-rich to permafrost with a decreasing level of ice is clearly visible on this plot. For granite, the alteration product is kaolinite characterized by $R = 0.20$ (Piolat *et al.* 2025). (b) Interpreted tomogram in normalized chargeability.

temperature remains the same as predicted by the theory. However, the presence of ice displays an equivalent chargeability higher than 1. This is only possible if other polarization mechanisms are coming into play such as strong low-frequency dielectric effects, which are known to exist for ice in presence of salts. We will not pursue further along this path in this paper. The main point is that in presence of massive ice, experiments show a strong and direct polarization associated with ice below the freezing point, in our model, likely associated with interfacial polarization as explained in our previous paper (Revil *et al.* 2025). Such phenomenon cannot be observed for crystalline rocks because the maximum amount of ice remains small with respect to the total volume of rock. With these observations in mind, we can now look further at the field data in Section 4 below.

Before going to the field data, we come back on the role of surface conductivity associated with alumina-silicates. In Fig. 12, we plot the surface conductivity versus the bulk component of the conductivity for the three samples used in this work and compare them to the results obtained in Revil *et al.* (2025). The question we want to address is what conductivity process (surface versus bulk) dominates the overall conductivity response of the three materials investigated in this study in freshwater conditions consistent with field conditions? Using the measured properties of Table 1, we clearly see in Fig. 12 that surface conductivity (associated mostly with clay minerals) is the dominant mechanism of electrical conduction through these porous media. This confirms again that surface conductivity cannot be neglected despite the assumption made in

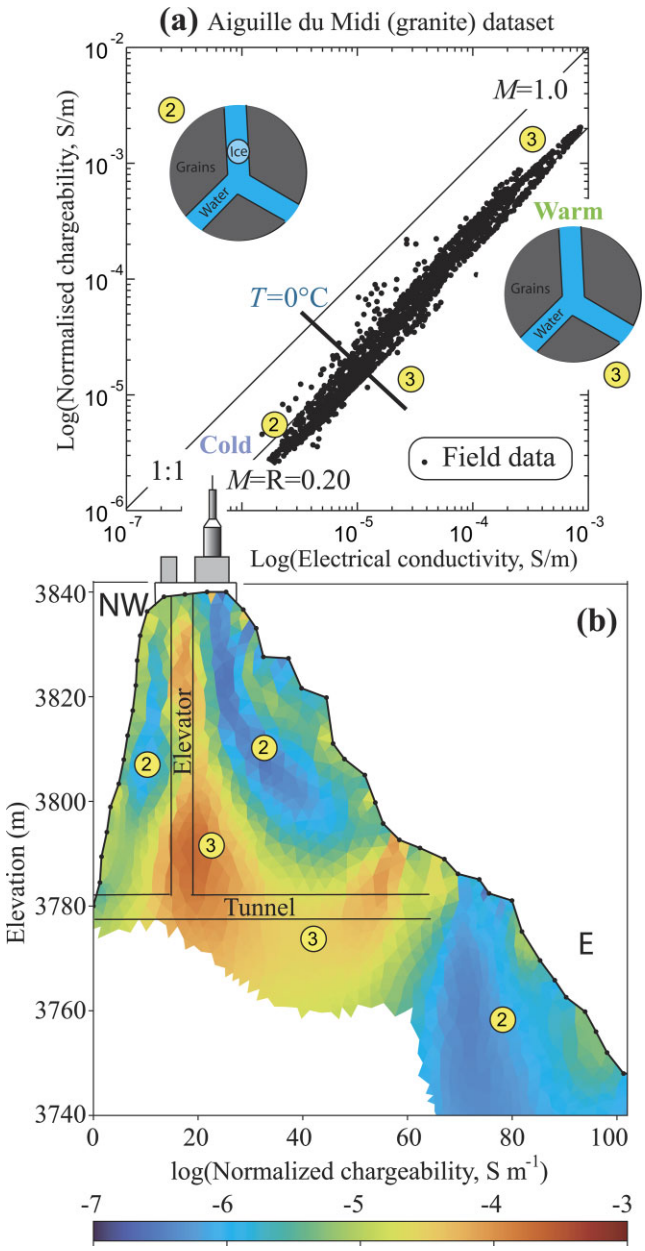

Figure 15. Site III (Aiguille du Midi, France). (a) Normalized chargeability *versus* electrical conductivity. The analysis of the data shows that there is only a small fraction of permafrost at the Aiguille du Midi. (b) Interpreted tomogram in normalized chargeability. The areas coloured in blue are designed to suggest the presence of permafrost in this area.

a growing number of studies (Wagner *et al.* 2019; Mollaret *et al.* 2020; Steiner *et al.* 2021, just to cite few of them).

4 INTERPRETATION OF THE FIELD DATA

4.1. Anatomy of the ice-rich areas

In Figs 13, 14 and 15, we plot the normalized chargeability versus the conductivity data from the three field sites. We use an amplification factor $a = 10$ prescribed by Piolat *et al.* (2025). The rational for this amplification factor is explained in details in Piolat *et al.* (2025) and will not be repeated here. We just mention that it is coming into play because the current injection time is not infinity but for a period $T = 1$ s, a dead time of 0.1 s and a recording time windows of 0.1 s for the first window sampling the decay curves (a slightly stronger amplification factor should be applied for a current injection period of 0.5 s). In Figs 14 and 15, the data aligned on $R = 0.20$ consistent with Piolat *et al.* (2025) for granite with kaolinite as alteration product. We recall that R is the ratio between the normalized chargeability and the conductivity and is also the ratio between λ and B (λ and B are the two mobilities used in DSL model, see Revil *et al.* 2025). This also indicates that the normalized chargeability and conductivity decreases the same way with the temperature below the freezing temperature and more importantly that surface conductivity dominates, once more, the overall conductivity response of the material.

At the opposite, Fig. 13 shows clearly the direct effect of ice because of high chargeabilities with values close to 1 indicating the presence of massive ice in agreement with field observations. The analysis of the data sets is used to see what areas are frozen or not, which could open the door to the use of clustering techniques to separate frozen and unfrozen areas or using neural networks to learn how to decipher such data set to reconstruct the temperature in Alpine areas. A preliminary step in this direction was proposed by Duvillard *et al.* (2021).

In Fig. 16, we analyse the histograms for the three field data set of the conductivity distribution shown for the tomograms displayed in Figs 13, 14 and 15. As suggested by Duvillard *et al.* (2021), the conductivity corresponding to the freezing point may be associated, under certain circumstances, with the minimum of these histograms. This observation finds its explanation with the strong change of slope associated with the conductivity versus temperature data set (as shown in Fig. 16d).

4.2. Determination of the water content and CEC

The DSL model discussed in Revil *et al.* (2025) is applied to obtain the tomograms of the water content θ and CEC for Sites I and II using the two following petrophysical transforms (see Piolat *et al.* 2025),

$$\theta = \left[\frac{1}{\sigma_w}\left(\sigma_\infty - \frac{M_n}{R}\right)\right]^{1/m}, \tag{2}$$

$$\mathrm{CEC} = \frac{a M_n}{\theta^{m-1}\rho_g \lambda}, \tag{3}$$

where σ_w (S m^{-1}) denotes the pore (liquid) water conductivity, σ_∞ and M_n are the conductivity and normalized chargeability from each cell of the corresponding tomograms (both in S m^{-1}), $R = 0.20$ (dimensionless parameter independent of temperature and saturation) for kaolinite and 0.10 for siliciclastic sediments (e.g. Piolat *et al.* 2025), $m = 1.5$ for granite (see Revil *et al.* 2025) and 2.0 for the siliciclastic sediments, $a = 10$ is the amplification factor for the corresponding parameters used in time-domain induced polarization (duration of the current injection time, dead time, times selected for the measuring window in the decay curve, see Piolat *et al.* 2025), $\rho_g = 2650$ kg m^{-3} for granite and siliciclastic sediments: for granite, Piolat *et al.* (2025) obtained $\lambda(\mathrm{Na}^+, 25°\mathrm{C}) = (1.7 \pm 0.5) \times 10^{-10}$ m^{2}s^{-1}V^{-1} and $R = 0.20$. This leads to $B(\mathrm{Na}^+, 25°\mathrm{C}) = \lambda(\mathrm{Na}^+, 25°\mathrm{C})/R = (0.85 \pm 0.3) \times 10^{-9}$ m^{2}s^{-1}V^{-1}. For silicoclastic sediments, we have $B(\mathrm{Na}^+, 25°\mathrm{C}) = 3.1 \times 10^{-9}$ m^{2}s^{-1}V^{-1}, $R = 0.10$ and therefore $\lambda(\mathrm{Na}^+, 25°\mathrm{C}) = 3.1 \times 10^{-10}$ m^{2}s^{-1}V^{-1}.

We apply the previous petrophysical transforms to Sites I to III and the results are displayed in Figs 17 to 19. In Fig. 18 (granodiorite

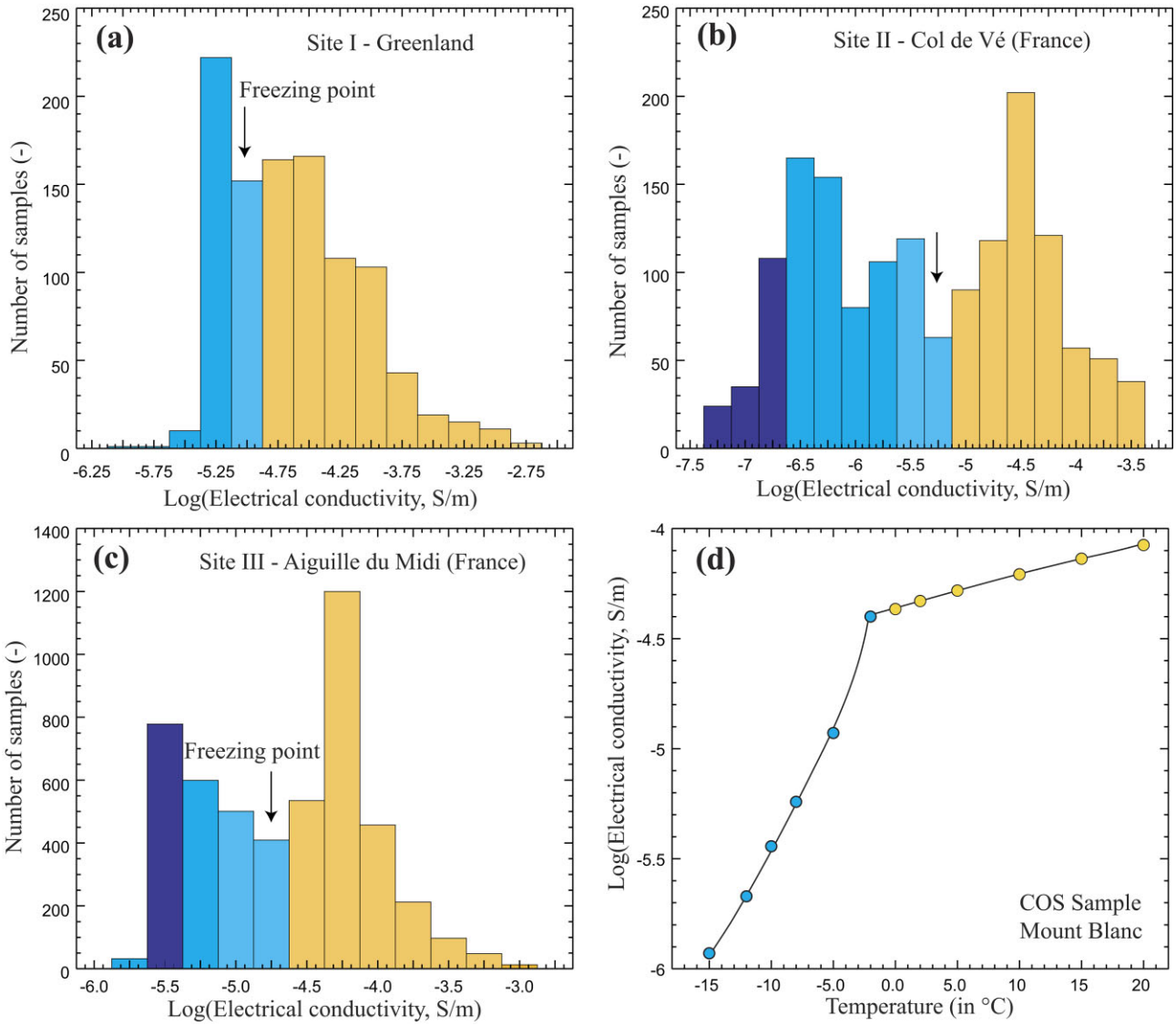

Figure 16. Determination of the freezing point from the histogram of the field data. (a) Histogram of the field data for Site. The minimum is hard to find because of the presence of different lithologies including high and low porosity materials. (b) Histogram of the field data for Site II (single lithology). (c) Histogram of the field data for Site III (single lithology). The conductivity corresponding to the freezing point is located at the first minima of the histogram for a given lithology. (d) Comparison with the laboratory data of a core sample of granite from the Mont-Blanc massif. Note that above the freezing point, this is the heterogeneity in the texture and surface properties that control the electrical conductivity distribution while below the freezing point, this is the temperature.

ridge of Greenland, the granite is characterized by a CEC of 0.1 meq/100 g). The Southern part, which is altered, is characterized by a CEC of ∼1 meq/100 g and the sand by a CEC of ∼2 meq/100 g. The two end-members (granitic sand and unaltered granite) are consistent with the porosity/CEC alteration path defined by Piolat *et al.* (2025) and shown in Fig.20

Then, we focus now on the CEC and water content of site II shown in Fig.18 The tomograms show the transition from the ice and rock mass overlying the marble substratum (South part of the profile) from the unfrozen sediments on the NW side of the profile. The water content tomograms shows a pocket of high water content below one of the lake present at the site and resulting from the melting of part of the permafrost at this site. The method could be therefore used to better monitor the fate of such water pockets at this site and elsewhere.

Fig. 19 shows the porosity and CEC tomograms for Site III (Aiguille du Midi). The range of values is grossly consistent with the values obtained on rock samples (porosity on the orders of 1 per cent and CEC around 1 meq/100 g, see Fig. 20). Close to the elevator and galleries, the values of the porosity and CEC are higher possibly due to the damaged zone surrounding galleries. Clearly the uncertainty in the drop of porosity from 1 per cent to 20 per cent is difficult to assess because of various sources of uncertainties such as the complex geometry of the site, the uncertainties associated with the inversion algorithm and the use of smoothing, and the uncertainty associated the petrophysical relationships and the input data. During the drilling of galleries, the release of the stress generates a fractured domain known as the excavation damaged zone (see Rutqvist *et al.* 2005; Tsang *et al.* 2005). The main implication related to the excavation damaged zone is the possibility of enhanced fracture flow parallel to the elevator and tunnel excavations. Fractures formed in the excavation damaged zone would enhance the fracture connectivity. The flow of the liquid water through this network of cracks and fractures in an area warmed by the heat brought

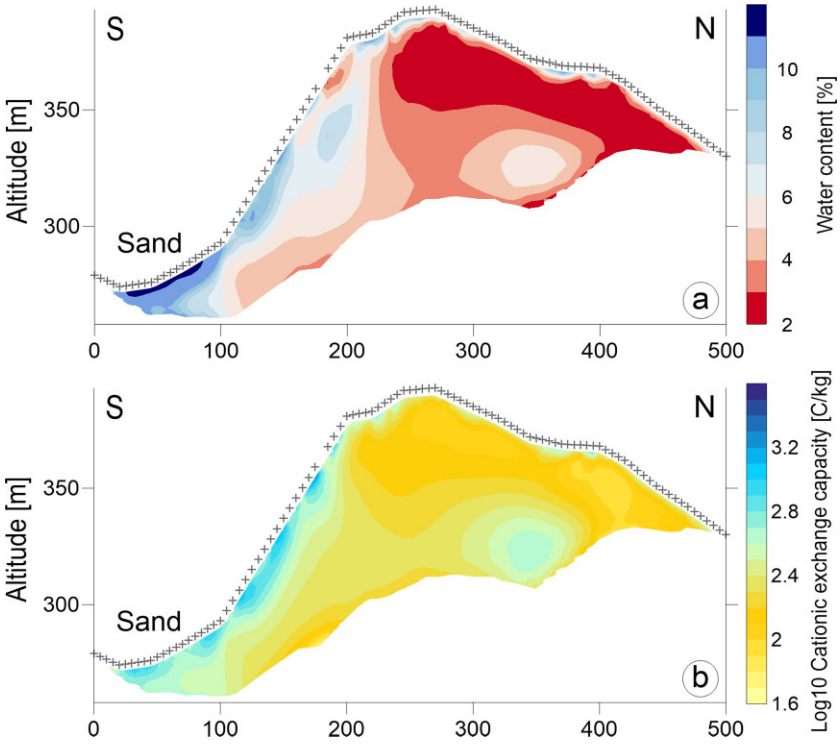

Figure 17. Interpreted results in terms of water content (volume fraction or per cent) and CEC (here in C kg^{-1}) along the 630 m profile at Site I. (a) Water content tomogram. (b) Cation exchange capacity (CEC) tomogram (expressed here in C kg^{-1} with 10^3 C $kg^{-1} \approx 1$ meq/100 g). Note that the South part of the ridge corresponds to a weathered granodiorite characterized by a higher CEC than the unaltered granodiorite.

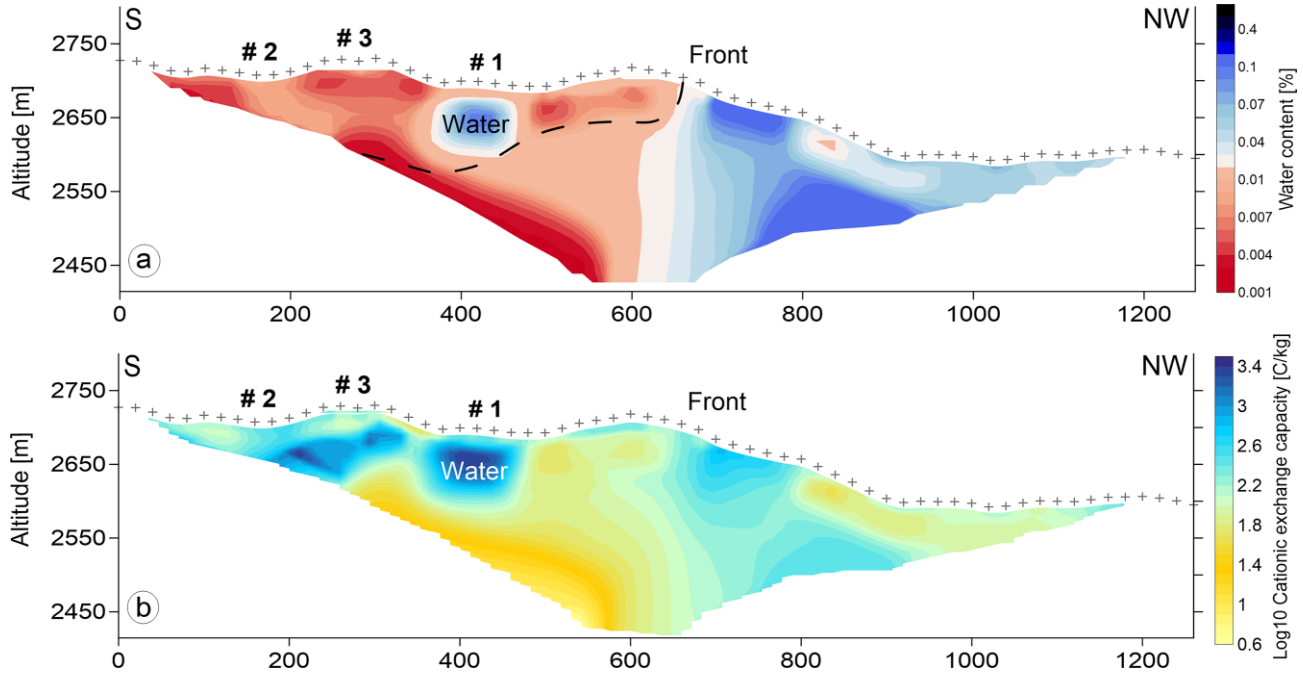

Figure 18. Interpreted results in terms of water content and CEC along the 1.26-km-long profile at Site II. (a) Water content tomogram (dimensionless). (b) Cation exchange capacity (CEC) tomogram (expressed here in C kg^{-1} with 10^3 C $kg^{-1} \approx 1$ meq/100 g).

through the tunnels and elevator may in turn increase of the alteration of the granite, which has been observed at short time scale in urban environments. Indeed, in presence of liquid water, the alteration of granites involves the transformation of primary minerals (mica and alkali feldspars) into secondary clay minerals especially kaolinite $Al_4(OH)_8[Si_4O_{10}]$. The alteration of minerals like orthoclase ($K[AlSi_3O_8]$, a potassium feldspar) and albite ($Na[AlSi_3O_8]$, a plagioclase) can be written as (Stoch & Sikora 1976; Nguetnkam

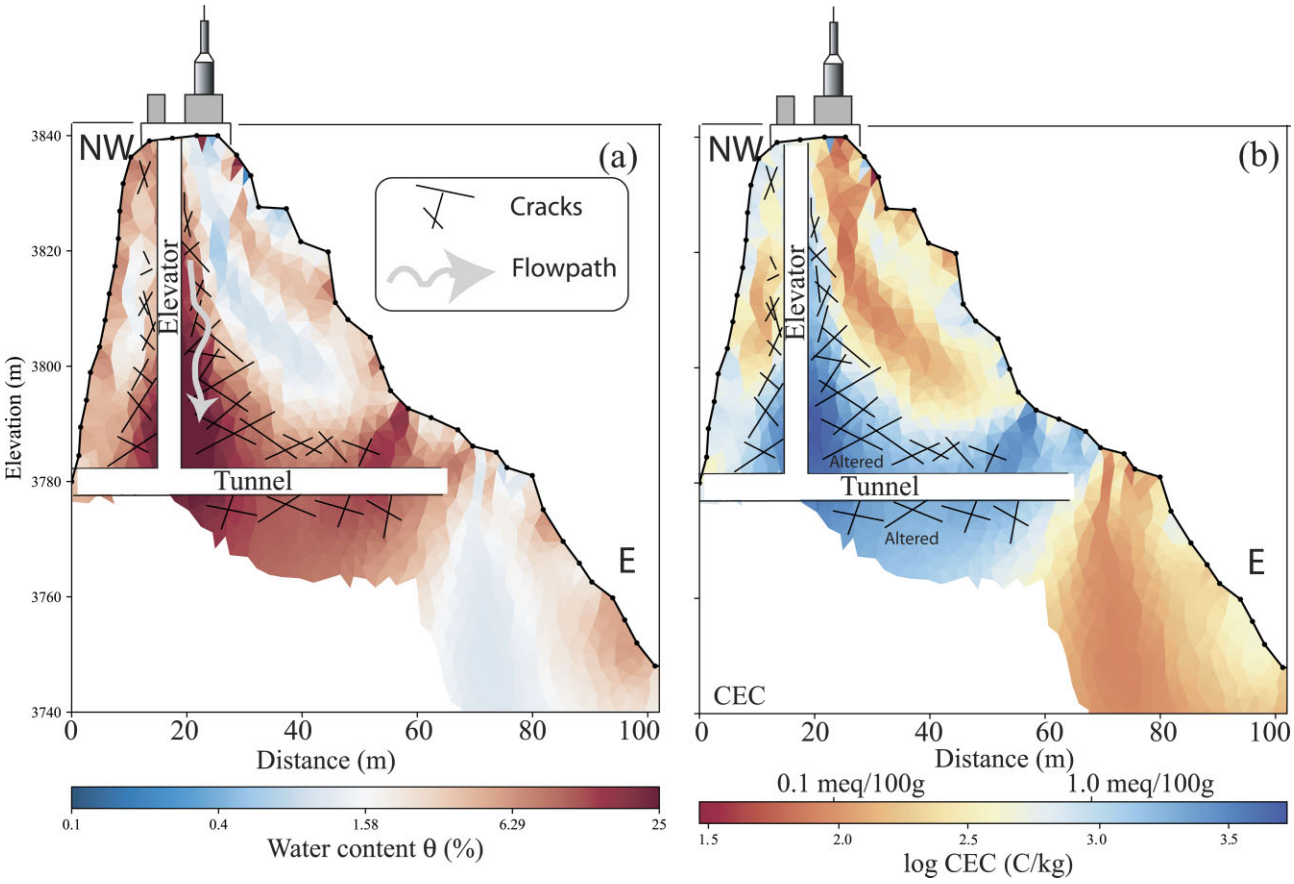

Figure 19. Interpreted tomograms in terms of water content and CEC at Site III (Aiguille du Midi). (a) Water content tomogram (here expressed in per cent). (b) Cation exchange capacity (CEC) tomogram (expressed here in C kg^{-1} with 10^3 C $kg^{-1} \approx 1$ meq/100 g). Pore water conductivity used as input parameter σ_w (25°C) = 0.026 S m^{-1}. The presence of an excavation damaged zone around the elevator and galleries seems clear on the tomograms.

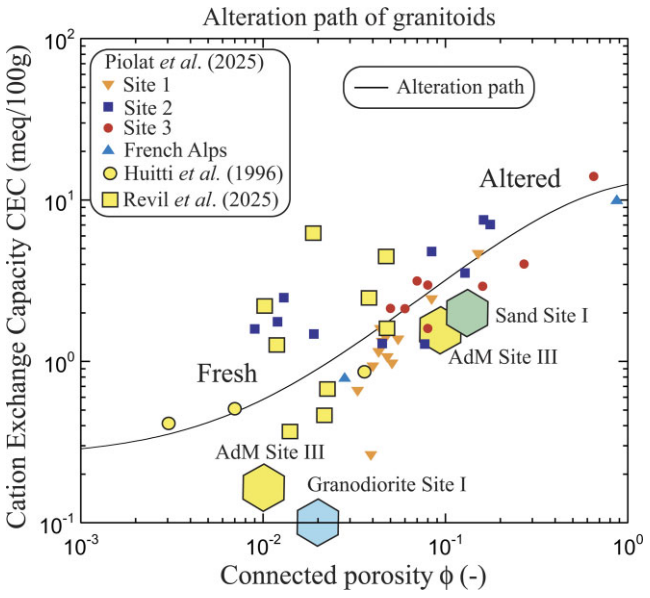

Figure 20. Observed alteration path between CEC and porosity ϕ of granites. The plain line corresponds to the fit of the following relationship CEC(meq/100g) $= m_1 + m_2(1 - \exp(-m_3\phi))$ corresponding therefore to the alteration path (essentially kaolinization, see details in Piolat *et al.* 2025) with $m_1 = 0.25 \pm 0.20$, $m_2 = 13 \pm 2$ and $m_3 = 2.5 \pm 0.9$ ($r^2 = 0.80$). Huitti *et al.* (1996) used three granite core samples characterized as fresh, weathered and altered and the CEC used here is reported for sodium Na^+.

et al. 2008):

$$4\text{Me}\,[AlSi_3O_8] + 4H_2O + 2CO_2 \Leftrightarrow \quad (4)$$
$$Al_4(OH)_8\,[Si_4O_{10}] + 2\text{MeCO}_3 + 8SiO_2.$$

In equation (4), Me = K, Na. Schiavon (2007) demonstrated that granite weathering leads to the formation of authigenic kaolinite in relatively short time-scales. This process can be accelerated in presence of SO_2 in acidic conditions. The increase of alteration of the granite would in turn increase the CEC of the rocks in the excavation damaged zone.

5 CONCLUSIONS

We have investigated the occurrence of permafrost at three very different sites both geologically and geomorphologically using the induced polarization method. Site I in Greenland is characterized by low-porosity crystalline rocks. Site II in the French Alps is characterized by a massive ice body in its upper part and a porous mixture of debris and ice in its lower part. This complex ice body is overlying a low porosity bedrock (marble). Site III also in the French Alps corresponds to a granitic peak. At each site, we acquired electrical resistivity and induced polarization measurements. After inversion, the data were displayed in terms of electrical conductivity, normalized chargeability and chargeability tomograms. The petrophysical model developed in the first paper of this series is applied to the determination of the liquid water content and CEC. The following results have been obtained.

(1) At Sites I and III, the direct effect of ice is not visible because of its small volume fraction related to the small porosity of the materials. When we plot the normalized chargeability *versus* the electrical conductivity, there is no change of slope of the trend indicating that the low frequency normalized chargeability and the conductivity follow the same trend with temperature below the freezing point.

(2) The presence of massive ice at the root of the rock glacier of Col des Vés gives high resistivities (in the range 1–20 Mohm m) and chargeability values close to 1. Ice is a dirty semiprotonic semiconductor but its surface properties should not be overlooked and the dependence of its surface conductance with frequency can explain the high polarizability of ice with chargeability values close to 1. This is the case here for high ice contents associated with a highly debris-covered glacier transitioning to a rock glacier with a high ice content and a decreasing ice content toward the front of the rock glacier.

(3) At Site III, the data are consistent with the data recorded in Greenland in terms of trend indicating a value of $R = 0.20$ consistent with the presence of kaolinite as alteration product. The presence of a borehole at Aiguille du Midi in which temperature was monitored and close to which resistivity were monitored can allow a comparison with the experimental data obtained in the laboratory. The comparison is good indicating that resistivity (and induced polarization) can be used to monitor temperature thanks to the exponential freezing curve developed by Duvillard *et al.* (2018) and discussed in the first paper of this series. Furthermore, the tomograms analysed in terms of porosity and CEC (used as a proxy for alteration) seem to evidence the presence of an excavation damaged zone around the elevator and galleries present at this site.

ACKNOWLEDGMENTS

We thank the CNRS for supporting this work and E. Zimmerman for the construction of two ZELSIP04-V02 impedance metres. The authors gratefully acknowledge the STGM (*Société des Téléphériques de la Grande Motte*) for the collaboration at the Col des Vés site. The research at Aiguille du Midi was funded by the ANR WISPER project (ANR-19-CE01-0018) and the Action Plan on Risks from Glacial and Periglacial Origin (PAPROG) from the French Ministry of Ecological Transition, Biodiversity, Forest, Sea and Fishing. We strongly thank the *Compagnie du Mont-Blanc* that provided access to the site and their support over the years. We thank T. Echelard, F. Hounkponou, G. Balestri, A.B. Abrahamsen, M. Cléritot, S. Alesina, A. Carlsen for their help during the field survey. G. Ménard, D. Cusicanqui, X. Bodin, S. Roudnitska are thanked for the fruitful discussions. The PhD thesis of JR is supported by a CIFRE grant with Naga Geophysics. The equipment used in this project was obtained thanks to the funding of the Auvergne-Rhône-Alpes region and FEDER through the IRICE project with the help of IRISK. IRISK is thanked for its strong support and fruitful discussions regarding gravitational instabilities over the years and especially Margot Bernard and François Nicot for their strong encouragements. The field campaigns to collect samples from Greenland were funded by the Nunatsinni Ilisimatusarnermik Siunnersuisoqatigiit (Greenland Research Council) and the Nordforsk ColdHUB project. AR thanks S. Missmahl for inspiration. This work is dedicated to Mike Batzle who was a great rock physicist and experimentalist at the Colorado School of Mines and a great, amazing, and funny friend (Mike we are missing you). We warmly thank the Editor, Alexis Maineult, and the two anonymous Referees for the high quality of their reviews and useful comments that have helped us to improve significantly and scientifically our manuscript.

DATA AVAILABILITY

The data used in this paper are available upon request to the corresponding author.

REFERENCES

Abdulsamad, F. *et al.* 2019. Complex conductivity of graphitic schists and sandstones, *J. geophys. Res.,* **124,** 8223–8249.

Abdulsamad, F. *et al.* 2025. Rockwall permafrost dynamics evidenced by automated electrical resistivity tomography at Aiguille du Midi (3842 m a.s.l., French Alps).

Abu-Hassanein, Z.S., Benson, C.H. & Blotz, L.R., 1996. Electrical resistivity of compacted clays, *J. Geotechn. Eng.,* **122,** 397–406.

Breede, K., Kemna, A., Esser, O., Zimmermann, E., Vereecken, H. & Huisman, J., 2011. Joint measurement setup for determining spectral induced polarization and soil hydraulic properties, *Vadose Zone J.,* **10**(2), 716–726.

Caranti, J.M. & Illingworth, A.J., 1983. Frequency dependence of the surface conductivity of ice, *J. Phys. Chem.,* **87**(21), 4078–4083.

Cathala, M. *et al.* 2024. Assessing the role of permafrost in the preconditioning and triggering factors of the September 2020 Crête des Grangettes rockfall (southern French Alps), *Géomorphologie: Relief Process. Environ.,* **30**(3), 171–188.

Clavier, C., Coates, G. & Dumanoir, J., 1977. The theoretical and experimental basis for the "dual-water" model for the interpretation of shaly sands, *Soc. Pet. Eng. Pap.,* **24,** 153.

Coperey, A., Revil, A., Abdulsamad, F., Stutz, B., Duvillard, P.A. & Ravanel, L., 2019. Low frequency induced polarization of porous media undergoing freezing: preliminary observations and modeling, *J. geophys. Res.,* **124,** 4523.

Dafflon, B., Hubbard, S., Ulrich, C., Peterson, J., Wu, Y.X., Wainwright, H. & Kneafsey, T.J., 2016. Geophysical estimation of shallow permafrost distribution and properties in an ice-wedge polygon-dominated Arctic tundra region, *Geophysics,* **81**(1), WA247–WA263.

Daigle, H., 2021. Structure of the electrical double layer at the ice–water interface, *J. Chem. Phys.,* **154,** 214703.

Doetsch, J., Ingeman-Nielsen, T., Christiansen, A.V., Fiandaca, G., Auken, E. & Elberling, B., 2015. Direct current (DC) resistivity and induced polarization (IP) monitoring of active layer dynamics at high temporal resolution, *Cold Reg. Sci. Technol.,* **119,** 16–28.

Duvillard, P.A. *et al.* 2025. La chapelle du Thabor (3165 m, Hautes-Alpes), un patrimoine sensible à l'évolution du permafrost de montagne, The Thabor chapel (3165 m.a.s.l., Hautes-Alpes), a heritage site vulnerable to changes in mountain permafrost, *Géomorphol. Relief Process. Environ.,* **30,** 3.

Duvillard, P.A., Magnin, F., Revil, A., Legay, A., Ravanel, L., Abdulsamad, F. & Coperey, A., 2021. Determining 2D temperature distribution in a permafrost-affected rock ridge from electrical conductivity tomography, *Geophys. J. Int.,* **225,** 1207–1221.

Duvillard, P.A., Revil, A., Qi, Y., Soueid, A.A., Coperey, A. & Ravanel, L. 2018. Three-dimensional electrical conductivity and induced polarization tomography of a rock glacier, *J. geophys. Res.,* **123,** 9528–9554.

Etzelmüller, B. *et al.* 2020. Twenty years of European mountain permafrost dynamics, the PACE legacy, *Environ. Res. Lett.,* **15**(10), 104070.d.

Fereydooni, H., Gruber, S., Cronmiller, D. & Stillman, D. 2024. Utilizing spectral induced polarization to identify the ice core of a pingo: a case study in Haines Junction, Yukon, Canada, in *12th International Conference on Permafrost,* Vol. **1,** pp. 87–93, eds. Beddoe, R.A. & Karunaratne, K.C., International Permafrost Association, Whitehorse, Canada, 16-20 June 2024.

Fereydooni, H., Gruber, S., Stillman, D. & Cronmiller, D., 2025. *Detecting Ground Ice in Warm Permafrost with the Dielectric Relaxation Time from SIP Observations,* EGUsphere.

Grimm, R.E., Stillman, D.E. & MacGregor, J.A., 2015. Dielectric signatures and evolution of glacier ice, *J. Glaciol.,* **61,** 1159.

Günther, T., Rücker, C. & Spitzer, K., 2006. Three-dimensional modelling and inversion of DC resistivity data incorporating topography-II. Inversion, *Geophys. J. Int.,* **166**(2), 506–517, August 2006.

Haeberli, W. *et al.* 2006. Permafrost creep and rock glacier dynamics, Permafrost, *Periglac. Process.,* **17**(3), 189–214.

Haeberli, W. & Fish, W., 1984. Electrical resistivity soundings of glacier beds: a test study, Grubengletscher, Wallis, Swiss Alps, *J. Glaciol.,* **30**(106), 373–376.

Hauck, C., Böttcher, M. & Maurer, H., 2011. A new model for estimating subsurface ice content based on combined electrical and seismic data sets, *Cryosphere,* **5,** 453–468.

Hauck, C., Isaksen, K., Vonder Mühll, D. & Sollid, J.L., 2004. Geophysical surveys designed to delineate the altitudinal limit of mountain permafrost: an example from Jotunheimen, *Permafrost Periglac. Process.,* **15,** 191–205.

Hauck, C., Vonder Mühll, D. & Maurer, H., 2003. Using DC resistivity tomography to detect and characterize mountain permafrost, *Geophys. Prospect.,* **51**(4), 273–284.

Henry, P. 1997. Relationship between porosity, electrical conductivity, and cation exchange capacity in Barbados wedge sediments, in *1997 Proceedings of the Ocean Drilling Program, Scientific Results,* Vol. **156,** eds. Shipley, T.H., Ogawa, Y., Blum, P. & Bahr, J.M., Texas A & M University, College station, TX, USA.

Herring, T. *et al.* 2023. Best practices for using electrical resistivity tomography to investigate permafrost, *Permafrost Periglac. Process.,* **34**(4), 494–512.

Herring, T., Cey, E. & Pidlisecky, A., 2019. Electrical resistivity of a partially saturated porous medium at subzero temperatures, *Vadose Zone J.,* **18,** 1.

Herring, T., Pidlisecky, A. & Cey, E., 2021. Removing the effects of temperature on electrical resistivity tomography data collected in partially frozen ground: limitations and considerations for field applications, *Vadose Zone J.,* **20,** e20146.

Hilbich, C., Marescot, L., Hauck, C., Loke, M.H. & Mäusbacher, R., 2009. Applicability of electrical resistivity tomography monitoring to coarse blocky and ice-rich permafrost landforms, *Permafrost Periglac.,* **20,** 269–284.

Huitti, T., Hakanen, M. & Lindberg, A. 1996. Sorption of cesium, radium, protactinium, uranium, neptunium and plutonium on rapakivi granite, Report Posiva-96-23. 28058692, 76pp.

Kemna, A. *et al.* 2012. An overview of the spectral induced polarization method for near-surface applications, *Near Surf. Geophys.,* **10,** 453–468.

Kemna, A., Vanderborght, J., Kulessa, B. & Vereecken, H., 2002. Imaging and characterisation of subsurface solute transport using electrical resistivity tomography (ERT) and equivalent transport models, *J. Hydrol.,* **267**(3–4), 125–146.

Kneisel, C., Hauck, C., Fortier, R. & Moorman, B., 2008. Advances in geophysical methods for permafrost investigations, *Permafrost Periglac. Process.,* **19,** 157–178.

Krautblatter, M., Verleysdonk, S., Flores-Orozco, A. & Kemna, A., 2010. Temperature-calibrated imaging of seasonal changes in permafrost rock walls by quantitative electrical resistivity tomography (Zugspitze, German/Austrian Alps), *J. geophys. Res.,* **115**.

Kulessa, B., Hubbard, B. & Brown, G., 2003. Cross-coupled flow modelling of coincident streaming and electrochemical potentials, and application to subglacial self-potential (SP) data, *J. geophys. Res.,* **108,** B8.

Kulessa, B., Hubbard, B., Williamson, M. & Brown, G., 2005. Hydrogeological analysis of slug tests in glacier boreholes, *J. Glaciol.,* **51,** 173, 269–280.

Kulessa, B., Murray, T. & Rippin, D., 2006, Active seismoelectric exploration of glaciers, *Geophys. Res. Lett.,* **33,** L07503.

Leloup, P.H., Arnaud, N., Sobel, E.R. & Lacassin, R., 2005. Alpine thermal and structural evolution of the highest external crystalline massif: the Mont Blanc, *Tectonics,* **24,** TC4002.

Lesmes, D.P. & Frye, K.M., 2001. Influence of pore fluid chemistry on the complex conductivity and induced polarization of Berea sandstone, *J. geophys. Res.,* **106**(B3), 4079–4090.

Loke., M.H., 2002. *RES2DINV, Ver. 3.50, Rapid 2-D Resistivity and IP Inversion Using the Least Square Method,* Geotomo Software, Penang. http://www.geoelectrical.com/contact.html.

Luo, H., Jost, A., Thiesson, J., Mendieta, A., Léger, E. & Jougnot, D., 2025. Induced polarization of clay under freeze-thaw cycling and desiccation processes: effect of surface cracking propagation, *Geophys. Res. Lett.,* **52,** e2024GL113424.

Luo, H.L., Jost, A., Thiesson, J., Mendieta, A., Léger, E. & Jougnot, D., 2024a. Dataset for "induced polarization of clay under freeze-thaw cycling and desiccation processes: effect of surface cracking propagation" (V1), *Zenodo*.

Luo, H.L., Jougnot, D., Jost, A., Teng, J.D., Mendieta, A., Lin, G. & Thanh, L.D., 2024b. Predicting the electrical conductivity of partially saturated frozen porous media, a fractal model for wide ranges of temperature and salinity, *Water Resour. Res.,* **60**(3), e2023WR034845.

Luo, H.L., Jougnot, D., Jost, A., Teng, J.D. & Thanh, L.D., 2023. A capillary bundle model for the electrical conductivity of saturated frozen porous media, *J. geophys. Res.: Solid Earth,* **128**(3), e2022JB025254.

Magnin, F., Deline, P., Ravanel, L., Noetzli, J. & Pogliotti, P., 2015b. Thermal characteristics of permafrost in the steep alpine rock walls of the Aiguille du Midi (Mont Blanc Massif, 3842 m a.s.l), *Cryosphere,* **9,** 109–121.

Magnin, F., Krautblatter, M., Deline, P., Ravanel, L., Malet, E. & Bevington, A., 2015a. Determination of warm, sensitive permafrost areas in near-vertical rockwalls and evaluation of distributed models by electrical resistivity tomography, *J. geophys. Res.,* **120,** 745–762.

Maierhofer, T., Hauck, C., Hilbich, C., Kemna, A. & Flores-Orozco, A., 2022. Spectral Induced Polarization imaging to investigate an ice-rich mountain permafrost site in Switzerland, *Cryosphere,* **16,** 1903–1925.

Marcer, M. *et al.* 2025. Regional patterns of mountain permafrost in Central West Greenland: a comparison between field data and regional models, in *Permafrost and PeriglacialProcesses*. (in press).

Marcer, M., Bodin, X., Brenning, A., Schoeneich, P., Charvet, R. & Gottardi, F., 2017. Permafrost favorability index: spatial modeling in the French Alps using a rock glacier inventory, *Front. Earth Sci.,* **5**.

Marcer, M., Duvillard, P.-A., Tomaškovičová, S., Nielsen, S.R., Revil, A. & Ingeman-Nielsen, T., 2024. Modelling present and future rock wall permafrost distribution in the Sisimiut mountain area, West Greenland, *Cryosphere,* **18,** 1753–1771. Copernicus GmbH.

Marcer, M., Serrano, C., Brenning, A., Bodin, X., Goetz, J. & Schoeneich, P., 2019. Evaluating the destabilization susceptibility of active rock glaciers in the French Alps, *Cryosphere,* **13,** 141–155.

Maurer, H. & Hauck, C., 2007. Geophysical imaging of alpine rock glaciers, *J. Glaciol.,* **53**(180), 110–120.

Mollaret, C., Hilbich, C., Pellet, C., Flores-Orozco, A., Delaloye, R. & Hauck, C. 2019. Mountain permafrost degradation documented through a network of permanent electrical resistivity tomography sites, *Cryosphere,* **13,** 2557–2578.

Mollaret, C., Wagner, F.M., Hilbich, C., Scapozza, C. & Hauck, C., 2020. Petrophysical joint inversion applied to alpine permafrost field sites to image subsurface ice, water, air, and rock contents, *Front. Earth Sci.,* **8,** 85.

Moore, J.C., Reid, A.P. & Kipfstuhl, J., 1994. Microstructure and electrical properties of marine ice and its relationship to meteoric ice and sea ice, *J. geophys. Res.: Oceans,* **99,** 5171–5180.

Moser, C., Morra di Cella, U., Hauck, C. & Flores Orozco, A., 2025. Spectral induced polarization survey for the estimation of hydrogeological parameters in an active rock glacier, *Cryosphere,* **19,** 143–171.

Mudler, J., Hördt, A., Kreith, D., Sugand, M., Bazhin, K., Lebedeva, L. & Radić, T. 2022. Broadband spectral induced polarization for the detection of permafrost and an approach to ice content estimation—a case study from Yakutia, Russia, *Cryosphere,* **16**(11), 4727–4744.

Nguetnkam, P., Kamga, R., Villiéras, F., Ekodeck, G.E. & Yvon, J., 2008. Variable weathering response of granite in tropical zones. Example of two sequences studied in Cameroon (Central Africa), *C. R. Geosci.,* **340**(7), 451–461.

Olhoeft, G.R., 1985, Low-frequency electrical properties, *Geophysics,* **50,** 2492–2503.

Olhoeft, G.R. & King, T.V.V., 1991. Mapping subsurface organic compounds noninvasively by their reactions with clays, *USGS Water Resources Investigation Report,* USGS, 91–4034.

Orsini, L. & Remy, J.-C., 1976. Utilisation du chlorure de cobaltihexamine pour la determination simultanée de la capacité d'échange et des bases échangeables des sols, *Science du Sol,* **4,** 269–275.

Petrenko, V. & Whitworth, R., 1999. *Physics of Ice,* Oxford Univ. Press.

Petrenko, V.F. & Ryzhkin, I.A., 1997. Surface states of charge carriers and electrical properties of the surface layer of ice, *J. Phys. Chem. B,* **101,** 6285–6289.

Piolat, L. *et al.* 2025. Induced polarization of volcanic rocks. 8. The case of intrusive igneous rocks, *Geophys. J. Int.,* **241,** 1348–1372.

Revil, A., 2012. Spectral induced polarization of shaly sands: influence of the electrical double layer, *Water Resour. Res.,* **48**.

Revil, A., 2013a. Effective conductivity and permittivity of unsaturated porous materials in the frequency range 1 mHz–1 GHz, *Water Resour. Res.,* **49,** 306–327.

Revil, A., 2013b. On charge accumulations in heterogeneous porous materials under the influence of an electrical field, *Geophysics,* **78**(4), D271–D291.

Revil, A. *et al.* 2017. Complex conductivity of soils, *Water Resour. Res.,* **53**(8), 7121–7147.

Revil, A. *et al.* 2022, Induced polarization images alteration in stratovolcanoes, *J. Volc. Geotherm. Res.,* **429,** 107598.

Revil, A. *et al.* 2025. Induced polarization as a tool to characterize permafrost. 1. Theory and laboratory experiments, *Geophys. J. Int.,* doi: 10.1093/gji/ggaf443.

Revil, A., Coperey, A., Deng, Y., Cerepi, A. & Seleznev, N., 2018. Complex conductivity of tight sandstones, *Geophysics,* **83**(2), E55–E74.

Rücker, C., Günther, T. & Wagner, F.M., 2017. pyGIMLi: an open-source library for modelling and inversion in geophysics, *Comput. Geosci.,* **109,** 106–123.

Rutqvist, J., Barr, D., Datta, R., Gens, A., Millard, M., Olivella, S., Tsang, C.F. & Tsang, Y. 2005. Coupled thermal-hydrological-mechanical analysis of the Yucca Mountain Drift Scale Test—comparison of field results to predictions of four different models, *Int. J. Rock Mech. Min. Sci.,* **42,** 680–697.

Schiavon, N., 2007. Kaolinisation of granite in an urban environment, *Environ. Geol.,* **52,** 399–407.

Steiner, M., Wagner, F.M., Maierhofer, T., Schoner, W. & Flores Orozco, A., 2021. Improved estimation of ice and water contents in Alpine permafrost through constrained petrophysical joint inversion: the Hoher Sonnblick case study, *Geophysics,* **86**(5), WB61–WB75.

Stillman, D., Robert, G. & Stephan, G., 2018. Spectral induced polarization surveys to infer ground ice in a peatland and a lithalsa in warm permafrost Near Yellowknife, Canada, in *5th European Conference on Permafrost,* Carleton University, Ottawa, Ontario, Canada. Available at: https://hdl.handle.net/20.500.14718/24109.

Stillman, D.E., Grimm, R.E. & Dec, S.F., 2010. Low-frequency electrical properties of ice—silicate mixtures, *J. Phys. Chem.,* **114,** 6065–6073.

Stillman, D.E., MacGregor, J.A. & Grimm, R.E., 2013a. The role of acids in electrical conduction through ice, *J. geophys. Res.,* **118,** 1–16.

Stillman, D.E., MacGregor, J.A. & Grimm, R.E., 2013b. Electrical response of ammonium-rich water ice, *Ann. Glaciol.,* **54**(64), 21–26.

Stoch, L. & Sikora, W., 1976. Transformation of micas in the process of kaolinisation of granites and gneisses, *Clays Clay Miner.,* **24,** 156–162.

Tsang, C.-F., Bernier, F. & Davies, C., 2005. Geohydromechanical processes in the Excavation Damaged Zone in crystalline rock, rock salt, and indurated and plastic clays—in the context of radioactive waste disposal, *Int. J. Rock Mech. Min. Sci.,* **42**(1), 109–125.

Vinegar, H.J. & Waxman, M.H., 1984. Induced polarization of shaly sands, *Geophysics,* **49,** 1267–1287.

Vonder Mühll, D., Hauck, C. & Gubler, H., 2002. Mapping of mountain permafrost using geophysical methods, *Prog. Phys. Geogr.: Earth Environ.,* **26,** 643–660.

Wagner, F.M., Mollaret, C., Gunther, T., Kemna, A. & Hauck, C., 2019. Quantitative imaging of water, ice and air in permafrost systems through petrophysical joint inversion of seismic refraction and electrical resistivity data, *Geophys. J. Int.,* **219**(3), 1866–1875.

Waxman, M.H. & Smits, L., 1968. Electrical conductivities in oil-bearing shaly sands, *Soc. Pet. Eng. J.,* **8**(2), 107–122.

Weller, A., Slater, L. & Nordsiek, S., 2013. On the relationship between induced polarization and surface conductivity: implications for petrophysical interpretation of electrical measurements, *Geophysics,* **78,** D315–D325.

Woodruff, W.F., Revil, A., Jardani, A., Nummedal, D. & Cumella, S., 2010. Stochastic inverse modeling of self-potential data in boreholes, *Geophys. J. Int.,* **183,** 748–764.

Zhou, Y., Li, G.-Y., Jin, H.-J., Marchenko, S.S., Ma, W., Du, Q.-S., Li, J.-M. & Chen, D., 2022. Viscous creep of ice-rich permafrost debris in a recently uncovered proglacial area in the Tianshan Mountains, China, *Adv. Clim. Change Res.,* **13,** 540.

Zimmermann, E., Kemna, A., Berwix, J., Glaas, W., Münch, H.M. & Huisman, J.A., 2008. A high-accuracy impedance spectrometer for measuring sediments with low polarizability, *Meas. Sci. Technol.,* **19**(10), 105603.